References

Balakrishnan, V., Becker, M., Lohrke, S., Nothwang, H.G., Guresir, E., Friauf, E., 2003. Expression and function of chloride transporters during development of inhibitory neurotransmission in the auditory brainstem. J. Neurosci. 23, 4134–4145.

Biwersi, J., Verkman, A.S., 1991. Cell-permeable fluorescent indicator for cytosolic chloride. Biochemistry 30, 7879–7883.

Chen, G., Trombley, P.Q., van den Pol, A.N., 1996. Excitatory actions of GABA in developing rat hypothalamic neurones. J. Physiol. 494, 451–464.

Cherubini, E., Gaiarsa, J.L., Ben-Ari, Y., 1991. GABA: an excitatory transmitter in early postnatal life. Trends Neurosci. 14, 515–519.

Clayton, G.H., Owens, G.C., Wolff, J.S., Smith, R.L., 1998. Ontogeny of cation–Cl^- cotransporter expression in rat neocortex. Brain Res. Dev. Brain Res. 109, 281–292.

DeFazio, R.A., Keros, S., Quick, M.W., Hablitz, J.J., 2000. Potassium-coupled chloride cotransport controls intracellular chloride in rat neocortical pyramidal neurons. J. Neurosci. 20, 8069–8076.

Di Cristo, G., Berardi, N., Cancedda, L., Pizzorusso, T., Putignano, E., Ratto, G.M., Maffei, L., 2001. Requirement of ERK activation for visual cortical plasticity. Science 292, 2337–2340.

Ehrlich, I., Lohrke, S., Friauf, E., 1999. Shift from depolarizing to hyperpolarizing glycine action in rat auditory neurones is due to age-dependent Cl^- regulation. J. Physiol. 520 (Pt 1), 121–137.

Fukuda, A., Tanaka, M., Yamada, Y., Muramatsu, K., Shimano, Y., Nishino, H., 1998. Simultaneous optical imaging of intracellular Cl^- in neurons in different layers of rat neocortical slices: advantages and limitations. Neurosci. Res. 32, 363–371.

Ganguly, K., Schinder, A.F., Wong, S.T., Poo, M., 2001. GABA itself promotes the developmental switch of neuronal GABAergic responses from excitation to inhibition. Cell 105, 521–532.

Geal-Dor, M., Freeman, S., Li, G., Sohmer, H., 1993. Development of hearing in neonatal rats: air and bone conducted ABR thresholds. Hear Res. 69, 236–242.

Gillen, C.M., Brill, S., Payne, J.A., Forbush III, B., 1996. Molecular cloning and functional expression of the K–Cl cotransporter from rabbit, rat, and human. A new member of the cation-chloride cotransporter family. J. Biol. Chem. 271, 16237–16244.

Grothe, B., Schweizer, H., Pollak, G.D., Schuller, G., Rosemann, C., 1994. Anatomy and projection patterns of the superior olivary complex in the Mexican free-tailed bat, *Tadarida brasiliensis* mexicana. J. Comp. Neurol. 343, 630–646.

Gulyas, A.I., Sik, A., Payne, J.A., Kaila, K., Freund, T.F., 2001. The KCl cotransporter, KCC2, is highly expressed in the vicinity of excitatory synapses in the rat hippocampus. Eur. J. Neurosci. 13, 2205–2217.

Haas, M., Forbush III, B., 1998. The Na–K–Cl cotransporters. J. Bioenerg. Biomembr. 30, 161–172.

Hensch, T.K., Fagiolini, M., Mataga, N., Stryker, M.P., Baekkeskov, S., Kash, S.F., 1998. Local GABA circuit control of experience-dependent plasticity in developing visual cortex. Science 282, 1504–1508.

Hollrigel, G.S., Soltesz, I., 1997. Slow kinetics of miniature IPSCs during early postnatal development in granule cells of the dentate gyrus. J. Neurosci. 17, 5119–5128.

Kaila, K., 1994. Ionic basis of GABAA receptor channel function in the nervous system. Prog. Neurobiol. 42, 489–537.

Kakazu, Y., Akaike, N., Komiyama, S., Nabekura, J., 1999. Regulation of intracellular chloride by cotransporters in developing lateral superior olive neurons. J. Neurosci. 19, 2843–2851.

Kakazu, Y., Uchida, S., Nakagawa, T., Akaike, N., Nabekura, J., 2000. Reversibility and cation selectivity of the K(+)–Cl(−) cotransport in rat central neurons. J. Neurophysiol. 84, 281–288.

Kandler, K., Friauf, E., 1995. Development of glycinergic and glutamatergic synaptic transmission in the auditory brainstem of perinatal rats. J. Neurosci. 15, 6890–6904.

Kapfer, C., Seidl, A.H., Schweizer, H., Grothe, B., 2002. Experience-dependent refinement of inhibitory inputs to auditory coincidence-detector neurons. Nat. Neurosci. 5, 247–253.

Kelsch, W., Hormuzdi, S., Straube, E., Lewen, A., Monyer, H., Misgeld, U., 2001. Insulin-like growth factor 1 and a cytosolic tyrosine kinase activate chloride outward transport during maturation of hippocampal neurons. J. Neurosci. 21, 8339–8347.

Kim, G., Kandler, K., 2003. Elimination and strengthening of glycinergic/GABAergic connections during tonotopic map formation. Nat. Neurosci. 6, 282–290.

Klinke, R., Kral, A., Heid, S., Tillein, J., Hartmann, R., 1999. Recruitment of the auditory cortex in congenitally deaf cats by long-term cochlear electrostimulation. Science 285, 1729–1733.

Kotak, V.C., Korada, S., Schwartz, I.R., Sanes, D.H., 1998. A developmental shift from GABAergic to glycinergic transmission in the central auditory system. J. Neurosci. 18, 4646–4655.

Koyano, K., Ohmori, H., 1996. Cellular approach to auditory signal transmission. Jpn. J. Physiol. 46, 289–310.

Luhmann, H.J., Prince, D.A., 1991. Postnatal maturation of the GABAergic system in rat neocortex. J. Neurophysiol. 65, 247–263.

Morishita, H., Makishima, T., Kaneko, C., Lee, Y.S., Segil, N., Takahashi, K., Kuraoka, A., Nakagawa, T., Nabekura, J., Nakayama, K., Nakayama, K.I., 2001. Deafness due to degeneration of cochlear neurons in caspase-3-deficient mice. Biochem. Biophys. Res. Commun. 284, 142–149.

Mossop, J.E., Wilson, M.J., Caspary, D.M., Moore, D.R., 2000. Down-regulation of inhibition following unilateral deafening. Hear Res. 147, 183–187.

Nabekura, J., Ebihara, S., Akaike, N., 1993. Muscarinic receptor activation of potassium channels in rat dentate gyrus neurons. J. Neurophysiol. 70, 1544–1552.

Nabekura, J., Omura, T., Akaike, N., 1996. Alpha 2 adrenoceptor potentiates glycine receptor-mediated taurine response through protein kinase A in rat substantia nigra neurons. J. Neurophysiol. 76, 2447–2454.

Nabekura, J., Ueno, T., Okabe, A., Furuta, A., Iwaki, T., Shimizu-Okabe, C., Fukuda, A., Akaike, N., 2002. Reduction of KCC2 expression and GABAA receptor-mediated excitation after in vivo axonal injury. J. Neurosci. 22, 4412–4417.

Nudel, U., Zakut, R., Shani, M., Neuman, S., Levy, Z., Yaffe, D., 1983. The nucleotide sequence of the rat cytoplasmic beta-actin gene. Nucleic Acids Res. 11, 1759–1771.

Payne, J.A., Rivera, C., Voipio, J., Kaila, K., 2003. Cation-chloride co-transporters in neuronal communication, development and trauma. Trends Neurosci. 26, 199–206.

Rajan, R., 1998. Receptor organ damage causes loss of cortical surround inhibition without topographic map plasticity. Nat. Neurosci. 1, 138–143.

Reid, K.H., Li, G.Y., Payne, R.S., Schurr, A., Cooper, N.G., 2001. The mRNA level of the potassium-chloride cotransporter KCC2 covaries with seizure susceptibility in inferior colliculus of the post-ischemic audiogenic seizure-prone rat. Neurosci. Lett. 308, 29–32.

Rittenhouse, C.D., Shouval, H.Z., Paradiso, M.A., Bear, M.F., 1999. Monocular deprivation induces homosynaptic long-term depression in visual cortex. Nature 397, 347–350.

Rivera, C., Voipio, J., Payne, J.A., Ruusuvuori, E., Lahtinen, H., Lamsa, K., Pirvola, U., Saarma, M., Kaila, K., 1999. The K^+/Cl^- co-transporter KCC2 renders GABA hyperpolarizing during neuronal maturation. Nature 397, 251–255.

Rohrbough, J., Spitzer, N.C., 1996. Regulation of intracellular Cl^- levels by Na(+)-dependent Cl^- cotransport distinguishes depolarizing from hyperpolarizing GABAA receptor-mediated responses in spinal neurons. J. Neurosci. 16, 82–91.

Sanes, D.H., Markowitz, S., Bernstein, J., Wardlow, J., 1992. The influence of inhibitory afferents on the development of postsynaptic dendritic arbors. J. Comp. Neurol. 321, 637–644.

Sanes, D.H., Takacs, C., 1993. Activity-dependent refinement of inhibitory connections. Eur. J. Neurosci. 5, 570–574.

Sanes, D.H., 1993. The development of synaptic function and integration in the central auditory system. J. Neurosci. 13, 2627–2637.

Sanes, D.H., Friauf, E., 2000. Development and influence of inhibition in the lateral superior olivary nucleus. Hear Res. 147, 46–58.

Suneja, S.K., Benson, C.G., Gross, J., Potashner, S.J., 1995. Evidence for glutamatergic projections from the cochlear nucleus to the superior olive and the ventral nucleus of the lateral lemniscus. J. Neurochem. 64, 161–171.

Thompson, S.M., Gahwiler, B.H., 1989. Activity-dependent disinhibition. II. Effects of extracellular potassium, furosemide, and membrane potential on ECl^- in hippocampal CA3 neurons. J. Neurophysiol. 61, 512–523.

Ueno, T., Okabe, A., Akaike, N., Fukuda, A., Nabekura, J., 2002. Diversity of neuron-specific K^+–Cl^- cotransporter expression and inhibitory postsynaptic potential depression in rat motoneurons. J. Biol. Chem. 277, 4945–4950.

Vale, C., Sanes, D.H., 2000. Afferent regulation of inhibitory synaptic transmission in the developing auditory midbrain. J. Neurosci. 20, 1912–1921.

Vale, C., Sanes, D.H., 2002. The effect of bilateral deafness on excitatory and inhibitory synaptic strength in the inferior colliculus. Eur. J. Neurosci. 16, 2394–2404.

Vale, C., Schoorlemmer, J., Sanes, D.H., 2003. Deafness disrupts chloride transporter function and inhibitory synaptic transmission. J. Neurosci. 23, 7516–7524.

Vater, M., 1995. Ultrastructural and immunocytochemical observations on the superior olivary complex of the mustached bat. J. Comp. Neurol. 358, 155–180.

Vu, T.Q., Payne, J.A., Copenhagen, D.R., 2000. Localization and developmental expression patterns of the neuronal K–Cl cotransporter (KCC2) in the rat retina. J. Neurosci. 20, 1414–1423.

Wiesel, T.N., Hubel, D.H., 1963. Single-cell responses in striate cortex of kittens deprived of vision in one eye. J. Neurophysiol. 26, 1003–1017.

Winer, J.A., Larue, D.T., Pollak, G.D., 1995. GABA and glycine in the central auditory system of the mustache bat: structural substrates for inhibitory neuronal organization. J. Comp. Neurol. 355, 317–353.

THE JOURNAL OF BIOLOGICAL CHEMISTRY
Vol. 279, No. 48, Issue of November 26, pp. 50619–50629, 2004
Printed in U.S.A.

Membrane-embedded C-terminal Segment of Rat Mitochondrial TOM40 Constitutes Protein-conducting Pore with Enriched β-Structure*

Received for publication, July 29, 2004, and in revised form, September 1, 2004
Published, JBC Papers in Press, September 3, 2004, DOI 10.1074/jbc.M408604200

Hiroyuki Suzuki‡§, Tomoko Kadowaki§¶, Maki Maeda‡, Hiroyuki Sasaki‖, Junichi Nabekura, Masao Sakaguchi‡‡, and Katsuyoshi Mihara‡§§**

*From the ‡Department of Molecular Biology, Graduate School of Medical Science, Kyushu University, Fukuoka 812-8582, the ¶Department of Pharmacology, Graduate School of Dental Science, Kyushu University, the ‖Department of Molecular Cell Biology, Institute of DNA Medicine, The Jikei University School of Medicine, Tokyo 105-8451, the **Department of Cellular and System Physiology, Graduate School of Medical Sciences, Kyushu University, Fukuoka 812-8582, and ‡‡Graduate School of Life Science, University of Hyogo, Ako Hyogo 678-1297, Japan*

TOM40 is the central component of the preprotein translocase of the mitochondrial outer membrane (TOM complex). We purified recombinant rat TOM40 (rTOM40), which was refolded in Brij35 after solubilization from inclusion bodies by guanidine HCl. rTOM40 (i) consisted of a 63% β-sheet structure and (ii) bound a matrix-targeted preprotein with high affinity and partially translocated it into the rTOM40 pore. This partial translocation was inhibited by stabilization of the mature domain of the precursor. (iii) rTOM40 bound preprotein initially through ionic interactions, followed by salt-resistant non-ionic interactions, and (iv) exhibited presequence-sensitive, cation-specific channel activity in reconstituted liposomes. Based on the domain structure of rTOM40 deduced by protease treatment, we purified the elastase-resistant and membrane-embedded C-terminal segment (rTOM40(ΔN165)) as a recombinant protein with 62% β-structure that exhibited properties comparable with those of full-size rTOM40. We concluded that the membrane-embedded C-terminal half of rTOM40 constitutes the preprotein recognition domain with an enriched β-structure, which forms the preprotein conducting pore containing a salt-sensitive *cis*-binding site and a salt-resistant *trans*-binding site.

Mitochondrial precursor proteins synthesized in the cytosol are delivered to the preprotein translocase of the outer membrane (TOM[1] complex) where the precursors destined to the inner compartments are translocated across the membrane, and those destined to the outer membrane are sorted into the lipid bilayer of the membrane (1–6). In yeast, the ~400-kDa TOM holocomplex is composed of the import receptors Tom70, Tom20, and Tom22, the import channel Tom40 with a predicted β-barrel structure, Tom 5, which regulates precursor transfer from the receptor to the channel, and Tom6 and Tom7, which regulate channel assembly (4, 7). Tom22, Tom5, Tom6, and Tom7 are tightly associated with Tom40 and form the ~350-kDa TOM core complex (7–9). The TOM holocomplex and TOM core complex exhibit two to three ring structures with an ~20-Å diameter and voltage-dependent, cation-specific channel activity (3, 8–10). The oligomeric form of *Neurospora crassa* Tom40 (~350 kDa), purified after dissociating the TOM holocomplex with dodecylmaltoside, is mainly composed of a one-ring structure with a 20–30-Å diameter (10) and exhibits channel activity comparable with that of the TOM core and holocomplexes. Upon reconstitution into liposomes, they actively import preproteins destined for the outer membrane, intermembrane space, inner membrane, and matrix (3, 11). Purified recombinant yeast Tom40 reconstituted into liposomes forms a cation-selective and voltage-dependent high conductance channel with multiple conductance states, which specifically bind mitochondria-targeting sequences added to the *cis*-side of the membrane (12). Matrix-targeted precursors or synthetic presequence peptides added to the *cis*-side strongly reduced the channel open probability and increased the frequency of channel gating. In a recent report, site-specific cross-linking revealed that the Tom40 channel binds to unfolded segments of non-native proteins and prevents their aggregation. Furthermore, it has the capacity to sequester ~90 residues of unfolded or loosely folded preproteins (13).

Despite these advances, mechanism of preprotein recognition and sorting by the Tom40 machinery remains unclear, probably due, partly, to the difficulty in isolating Tom40 in the correctly folded and soluble form. In the present study, we expressed rat mitochondrial TOM40 (rTOM40) (14) in *Escherichia coli*, and we purified it from the inclusion bodies by solubilizing it in 6 M guanidine hydrochloride (GdnHCl) with subsequent refolding in the non-ionic detergent Brij35. The purified rTOM40 consisted of a ~63% β-structure and, when incorporated into liposomes, exhibited presequence-sensitive, cation-specific channel activity. A pull-down assay and surface plasmon resonance (SPR) revealed that purified rTOM40 directly bound loosely folded matrix-targeted preprotein, pSU9-DHFR, with high affinity (K_D range of 10^{-10}). Salt sensitivity of the binding indicated that rTOM40 recognized preproteins by two distinct sequential interactions: initial ionic interactions

* This work was supported by grants from the Ministry of Education, Science, and Culture of Japan (to M. S. and K. M.), from the Takeda Science Foundation, Core Research from Evolutional Science and Technology, and Specially Promoted Research from the Ministry of Education, Science, and Culture of Japan (to K. M.). The costs of publication of this article were defrayed in part by the payment of page charges. This article must therefore be hereby marked "*advertisement*" in accordance with 18 U.S.C. Section 1734 solely to indicate this fact.

§ Both authors contributed equally to this work.
§§ To whom correspondence should be addressed. Tel.: 81-92-642-6176; Fax: 81-92-642-6183; E-mail: mihara@cell.med.kyushu-u.ac.jp.

[1] The abbreviations used are: TOM, translocase of outer membrane; GdnHCl, guanidine hydrochloride; MPP, mitochondrial processing peptidase; pAd, preadrenodoxin; preSU9-DHFR, a construct in which a 1–69 segment of precursor for subunit 9 of *N. crassa* F_1-ATPase was fused to the N terminus of dihydrofolate reductase; SPR, surface plasmon resonance; HA, hemagglutinin; PMSF, phenylmethylsulfonyl fluoride; 2ME, 2-mercaptoethanol; rTOM40, recombinant rat TOM40; Ni-NTA, nickel-nitrilotriacetic acid; mAd, mature form of adrenodoxin.

followed by salt-resistant hydrophobic interactions. These sequential interactions drove partial translocation of preproteins and sequestration of the mitochondrial processing peptidase (MPP)-processing site of preproteins within the rTOM40 pore. We then narrowed the location of the β-structure-enriched channel domain to the membrane-embedded C-terminal half of rTOM40 (residues 166–361). Purified recombinant rTOM40(ΔN165) was in the oligomeric form of ~170-kDa, as assessed by gel filtration, and exhibited both structural and preprotein-binding characteristics almost identical to those of rTOM40.

EXPERIMENTAL PROCEDURES

Plasmid Constructions—For construction of the *E. coli* expression plasmid of rat TOM40, the 1086-bp cDNA encoding N-terminal His_6-tagged TOM40 was cloned into the NdeI-BamHI sites of pET28a (Novagen) to obtain pET28-NHis40 (14). The expression vector of rTOM40(ΔN165) was constructed as follows. A DNA fragment encoding His_6-TOM40(ΔN165) was prepared by PCR using pET28a-NHis40 as the template, and the following oligonucleotides as the primer: sense strand, 5′-GGGAATTCCATATGCACCAGCTGAGCCCAG GC-3′, and antisense strand, 5′-GCGGGATCCTCAGCCGATGGTGAG GCC AAA-3′. The NdeI and BamHI sites are underlined. The fragment was inserted into the NdeI-BamHI sites of pET28a to create pET28a-ΔN165. The expression vector for the N-terminal His_6-tagged TOM40-(1–165) was constructed as follows. A DNA coding for N-terminal His_6-tagged TOM40-(1–165) was amplified by PCR using pET28-NHis40 as the template and the following oligonucleotides as the primers: sense strand, 5′-GGGAATTCCATATGGGGAACGTGTTGGCTGCT-3′, and antisense strand, 5′-GCGGGATCCTCAGATGACCTGTGCATTGAG-3′. The NdeI and BamHI sites are underlined. The amplified fragment was inserted between the NdeI-BamHI sites of pET28a to create pET28a-(1–165).

Purification of rTOM40, rTOM40(ΔN165), and rTOM40-(1–165)—BL21(DE3)LysS cells harboring the expression plasmids for rTOM40, rTOM40(ΔN165), or rTOM40-(1–165) were cultured to A_{600} = 0.5, and protein expression was induced by 1 mM isopropyl 1-thio-β-D-galactopyranoside and cultured further for 3 h at 30 °C. The cells were suspended in the sonication buffer (50 mM Tris-HCl (pH 7.5) containing 250 mM NaCl, 1 mM EDTA, and 1 mM PMSF) and disrupted by sonication. For purification of rTOM40-(1–165), the soluble supernatant fraction obtained by ultracentrifugation was directly applied to a HiTrap chelating HP column (Amersham Biosciences). For purification of rTOM40 and rTOM40(ΔN165), the sonicated cell debris was washed with sonication buffer containing 1% Triton X-100, and the unsolubilized fraction was recovered by centrifugation. This step was repeated nine times, and the unsolubilized materials were washed once with 20 mM Tris-HCl (pH 7.5) containing 500 mM NaCl, 4 M urea, and 1 mM PMSF. After centrifugation, the obtained inclusion bodies were suspended in the lysis buffer (20 mM Tris-HCl buffer (pH 8.0), containing 0.5 M NaCl, 6 M guanidine HCl, 1 mM 2-mercaptoethanol (2ME), and 5 mM imidazole). The ultracentrifuged supernatant was passed through a HiTrap chelating HP column equilibrated with the lysis buffer. The column was extensively washed with washing buffer (20 mM Tris-HCl (pH 8.0) containing 0.5 M NaCl, 6 M urea, 1 mM 2ME, and 5 mM imidazole), and then the washing buffer was slowly exchanged (0.2 ml/min) by a concentration gradient from 0 to 100% of the refolding buffer (20 mM Tris-HCl (pH 8.0) containing 0.5 M NaCl, 0.5% Brij35, 1 mM 2ME). After the refolding step, rTOM40 or rTOM40(ΔN165) was eluted by 20 mM Tris-HCl buffer (pH 8.0) containing 0.5 M NaCl, 0.5% Brij35, 1 mM 2ME, and 300 mM imidazole. The eluted fraction was applied to a Mono-S column equilibrated with 20 mM phosphate buffer (pH 6.5) containing 0.5% Brij35, and eluted by a 0 to 1 M NaCl concentration gradient in the same buffer. The eluted proteins were dialyzed against 20 mM sodium phosphate buffer (pH 7.0) containing 0.5% Brij35. Approximately 5 mg of rTOM40 or rTOM40(ΔN165) was obtained in high purity from ~15 g (wet weight) of *E. coli* cells.

Preparation of Elastase Fragments of rTOM40 for the N-terminal Sequencing—The reaction mixture (50 μl) containing 3 μg of rTOM40 and elastase (2 μg/ml) was incubated at 0 °C for 30 min. The protein fragments were recovered by trichloroacetic acid precipitation and separated by SDS-PAGE. The fragments were transferred to polyvinylidene difluoride membrane followed by Ponceau S-staining. The stained bands were cut out and subjected to protein sequencing.

Preparation of Proteoliposomes—Preparation of proteoliposomes containing rTOM40 was essentially according to the method described by Jackson and Litman (15). Briefly, 1.2 mg of L-α-phosphatidylcholine and 0.8 mg of L-α-phosphatidylethanolamine in chloroform were mixed in a test tube, and the solvent was evaporated by flushing with N_2. One milliliter of 50 mM Tris-HCl buffer (pH 7.5) containing 0.5% Brij35 and 20 μg of rTOM40 was added to the tube, vortexed, and incubated on ice for 4 h with intermittent mixing. After incubation, the reaction mixture was diluted in 50 ml of 50 mM Tris-HCl buffer (pH 7.5) containing 50 mM sodium acetate. The reaction mixture was then dialyzed against 5 liters of 10 mM Tris-HCl buffer (pH 7.5) containing 0.15 M NaCl and 20 g of Bio-Beads SM-2 (Bio-Rad). The dialysate was concentrated using a membrane filter. Approximately 80% of the obtained proteoliposomes assumed unilamellar vesicles with ~0.1 μm diameter.

Preparation of Mitochondria from HeLa Cells Expressing the Epitope-tagged rTOM40—HeLa cells were transfected with N-terminal His_6-tagged rTOM40 or C-terminal HA-tagged rTOM40 using FuGENE 6 (Roche Applied Science) and cultured for 24 h. The cells were collected and homogenized in the homogenization buffer (10 mM Hepes-KOH buffer (pH 7.4), containing 0.22 M mannitol, 0.07 M sucrose, and 1 mM PMSF) by passing them through a 27-gauge needle 20 times using a syringe. The homogenate was centrifuged at 600 × *g* for 5 min, and the supernatant was then centrifuged at 6000 × *g* for 10 min to obtain the mitochondrial fraction.

Measurement of Channel Activity—Electrical measurements were performed with nystatin-perforated patch recordings applied on lipid bilayer vesicles containing rTOM40. SCC1–19 (10 μM) dissolved in the perfusate was applied using the Y-tube method, which allowed the external solution to be exchanged within 20 ms (16). The resistance between the patch pipette and the reference electrode in the external solution was 10–12 megohms. Ionic currents were measured with a patch clamp amplifier (EPC-7, List-Medical, Germany) and low pass filtered at 1 kHz (E-3210A, NF Electronic Instruments, Japan). All experiments were performed at room temperature. The composition of the pipette solution was 100 mM KCl, 50 mM potassium methane sulfonate, and 10 mM Hepes (pH 7.2). The external solution contained 150 mM KCl, 10 mM Hepes (pH 7.2), and 1 mM $CaCl_2$. In some experiments, the reversal potentials were obtained as the membrane potential at which the current responses to ramp voltage steps from −100 mV to +100 mV with and without SCC1–19 intersected with each other. The presence of the TOM40 pore was verified by measuring release of [^{14}C]sucrose from the proteoliposomes containing rTOM40 or rTOM40(ΔN165). The assay was carried out essentially as described by Zalman *et al.* (17) using [^{14}C]sucrose and [^{3}H]dextran (mean M_r, 70,000) as the permeable and impermeable substrates, respectively, except that rTOM40, rTOM40(ΔN165), rTOM40-(1–165), or lactate dehydrogenase, in lieu of mitochondrial outer membrane, was reconstituted into asolectin liposomes. The reaction mixture was passed through a Sepharose CL-4B column (0.9 × 9.5 cm) equilibrated with 10 mM Hepes-KOH buffer (pH 7.4) containing 100 mM NaCl, 0.1 mM $MgCl_2$, and 3 mM NaN_3. 0.3-ml fractions were collected and assayed for radioactivity by using a liquid scintillation counter. Membrane vesicles were eluted in fractions 6–7 (Fig. 7*B*).

Isolation of Proteoliposomes by Centrifugal Floatation—After reconstitution of proteoliposomes, the reaction mixture was adjusted to 1.6 M sucrose, placed under the layers of 1.25 M and 0.25 M sucrose, and centrifuged in a Hitachi RP-S120AT3 rotor at 100,000 rpm for 90 min. Proteoliposomes floated to the 0.25 and 1.25 M sucrose layers were recovered and analyzed by SDS-PAGE.

Binding Assay of Preproteins to rTOM40, rTOM40(ΔN165), or rTOM40-(1–165) by Co-precipitation—The mixture containing 1 μg of pAd and the indicated amounts of rTOM40, rTOM40(ΔN165), or rTOM40-(1–165) in 200 μl of the binding buffer (20 mM Hepes-KOH buffer (pH 7.4) containing 0.1% Brij35, and 50 mM NaCl) was incubated at 30 °C for 30 min. The reaction mixture was centrifuged at 45,000 rpm for 5 min. The obtained supernatant was mixed with 30 μl (50% slurry) of TALON metal affinity resin (Clontech) and incubated at 4 °C for 1 h. The beads were washed with the binding buffer, and the bound proteins were analyzed by SDS-PAGE and subsequent immunoblotting using anti-adrenodoxin IgG.

Protection of the MPP-processing Site of pAd by rTOM40 or rTOM40(ΔN165)—Binding of pAd to rTOM40, rTOM40(ΔN165), or rTOM40-(1–165) and isolation of the complex by TALON beads were performed as described above. The isolated beads were suspended in 25 μl of the binding buffer, and the suspension was then incubated with 3 μg of yeast recombinant MPP in the presence of 2 mM MnCl2 at 30 °C for 30 min. The reaction was terminated with the sample loading buffer and analyzed by SDS-PAGE and subsequent immunoblotting using anti-adrenodoxin IgG.

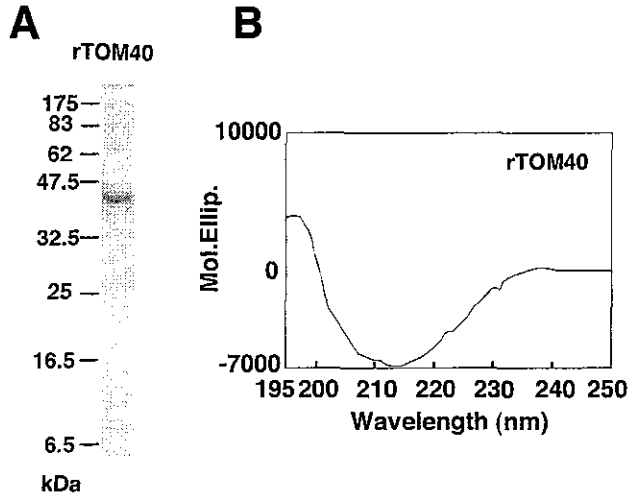

FIG. 1. **Structural characteristics of rTOM40.** *A*, SDS-PAGE profile of purified rTOM40. *B*, CD spectrum of rTOM40.

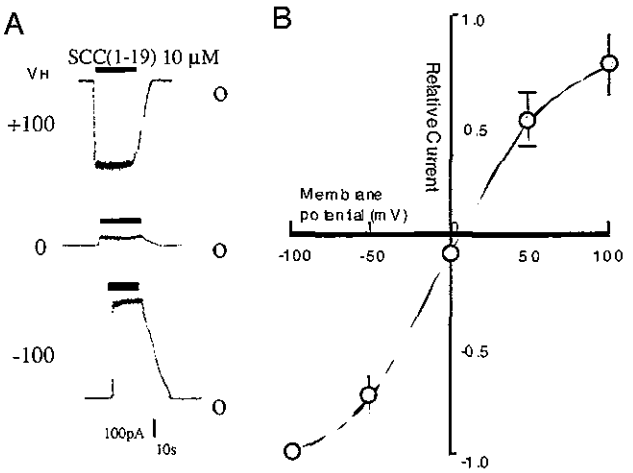

FIG. 2. **Kinetics and reversal potential of presequence peptide-sensitive current of the rTOM40 channel.** *A*, the presequence peptide-induced shift of the current level. *B*, relative current as a function of applied membrane potential. Electrical measurements were performed as described under "Experimental Procedures."

CD Spectrum Measurement—CD spectra of rTOM40, rTOM40(ΔN165), and rTOM40-(1–165) were measured in 10 mM Tris-HCl buffer (pH 7.4) containing 0.5% Brij35 at 25 °C using a JASCO J-720 spectropolarimeter and a cuvette with a 1-mm light-path. Each spectrum represents an average of five scans from 195 to 250 nm at 0.1-nm intervals. The base line was established by subtracting the spectrum of the buffer alone. Analysis of the secondary structure was performed using the method of Reed and Reed (18).

Surface Plasmon Resonance Measurements—The SPR measurements were performed at 25 °C with a Biacore 3000 (Biacore AB). Purified rTOM40, rTOM40(ΔN165), or rTOM40-(1–165) was immobilized onto the sensor chip CM5 by amine-coupling according to the manufacturer's protocol. Briefly, the coupling was performed in 10 mM sodium acetate buffer (pH 6.5) at a protein concentration of 10 μg/ml. The level of immobilization typically corresponded to 2000 resonance units, which corresponded to ~2 ng of protein/mm^2 (Fig. 6, *A–D*). In Fig. 6*E*, rTOM40 was immobilized to the chip at 22,000 resonance units (corresponding to ~22 ng of protein/mm^2). Binding analyses were performed in 20 mM Hepes-KOH buffer (pH 7.4) containing 150 mM NaCl and 0.05% Brij35 (running buffer) at a flow rate of 20 μl/min. The sensor chip surface was regenerated by 50 mM HCl. Binding curves were analyzed using BIA-Evaluation software (version 3.2). The kinetic data fitting was performed using a Langmuir 1:1 binding model.

RESULTS

Purification of Rat TOM40—N-terminal His_6-tagged rTOM40 expressed in *E. coli* as inclusion bodies was solubilized by 6 M GdnHCl, applied to a Ni-NTA affinity column, and subjected to a refolding reaction by exchanging GdnHCl slowly with Brij35. rTOM40 was then eluted by imidazole and subjected to Mono-S column chromatography. Purified rTOM40 (Fig. 1*A*) was eluted through a Superose 6 column with a peak at ~250 kDa, although with a rather broad elution profile (see Fig. 5*B*).

Secondary Structure of rTOM40—A CD spectrum of rTOM40 in 0.5% Brij35 had a minimum value at 213 nm, crossover of the base line at 201 nm, and zero ellipticity at a wavelength 235 nm (Fig. 1*B*). The secondary structure of rTOM40 estimated from the CD spectrum using the program of Reed and Reed (18) comprised 62.9% β-sheet, 10.0% α-helix, 5.9% turn, and 21.1% random structures in the protein. The content of the β-sheet structure of rTOM40 was comparable with that of recombinant *Saccharomyces cerevisiae* Tom40 (>60%) purified from inclusion bodies after solubilization with 8 M urea and either reconstituted into liposomes or solubilized in Mega9, although the CD spectra were distinct (12). The secondary structure of rTOM40 was significantly different from that of the oligomeric form of *N. crassa* Tom40, which was purified after dissociation of the purified TOM complex with octyl glucoside (less β-sheet, ~31%; more α-helix, 30%) (10). The reason for this structural difference between rat and *N. crassa* Tom40 is not known.

Channel Properties of rTOM40—The purified TOM holocomplex, TOM core complex, oligomeric *N. crassa* Tom40 isolated from the purified TOM core complex, and recombinant Tom40 of *S. cerevisiae* form cation-selective high conductance channels when incorporated into lipid membranes and the presequence peptide block the channel in a voltage-dependent manner (3, 8, 10, 12, 19). We therefore examined whether purified rTOM40 was correctly folded to exhibit channel activity. rTOM40 was incorporated into unilamellar ~0.1-μm-diameter liposomes, and electrical measurements were performed with nystatin-perforated patch recordings. A functional presequence peptide SCC1–19 (10 μM) (20) induced an immediate outward shift of current at a holding potential of −100 mV in less than 1 s (Fig. 2). During SCC1–19 application, there was no desensitization of the current but current noise increased. The current returned to base line within 10 s upon washing out the presequence peptide. Less hyperpolarization of the membrane reduced SCC1–19-induced current amplitude and a positive membrane potential reversed the direction of SCC1–19-induced current inward. The reversal potential of SCC1–19-induced current was 8.3 ± 3.2 mV (mean ± S.E., n = 5). This result suggested that the lipid bilayer with rTOM40 contains cation-permeable ion channels that are rapidly and reversibly blocked by the presequence peptide.

Binding of Matrix-targeted Preproteins to Purified rTOM40—Confirming that recombinant rTOM40 had refolded to constitute a dominant β-sheet structure and to exhibit channel activity, we examined its interaction with matrix-targeted preproteins. Recombinant preadrenodoxin (pAd) (21) was incubated with rTOM40 (N-terminal His_6-tagged), and rTOM40 was recovered with nickel resin. Immunoblot analysis with anti-adrenodoxin antibody revealed that pAd was recovered to the nickel resin depending on the amount of rTOM40 added to the reaction mixture (Fig. 3*A*). As a control, the mature form of adrenodoxin (mAd) did not bind to rTOM40 (data not shown). The interaction between rTOM40 and pAd was sensitive to NaCl, and the interaction was almost completely abolished by 500 mM NaCl (Fig. 3*B*). The pAd·rTOM40 complex, once formed, was stable in high salt (Fig. 3*B*, *Af* in the *lower panel*). These results suggested that the preprotein initially binds to rTOM40 mainly through ionic interactions, which is followed

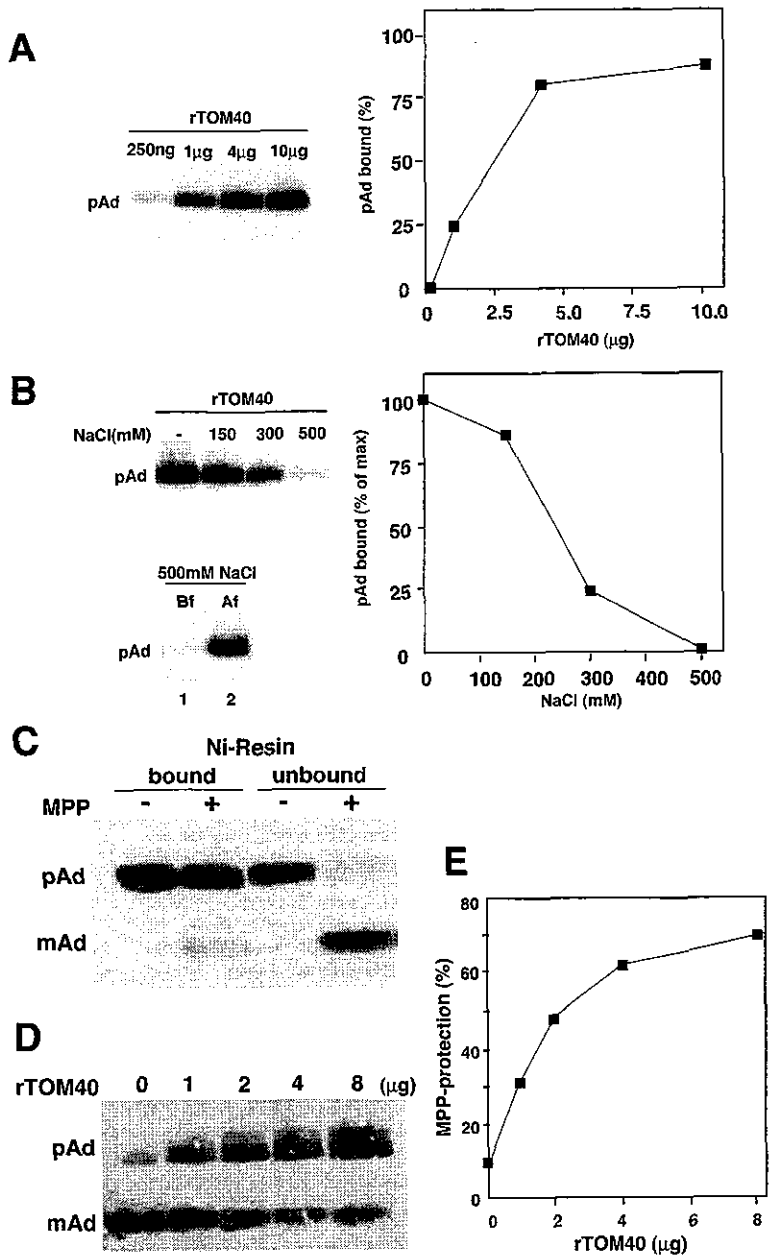

FIG. 3. **Recognition of preprotein by purified rTOM40.** *A*, binding of pAd to rTOM40 as measured by pull-down assay. pAd (1 μg) was incubated with the indicated amounts of rTOM40 (N-terminal His_6-tagged), and then the reaction mixtures were subjected to pull-down reaction by Ni-NTA beads. The recovered pAd·rTOM40 complex was subjected to SDS-PAGE followed by immunoblotting using anti-adrenodoxin antibodies and subsequent image analysis by a LAS1000 *plus* (Fuji Film Co.). The band intensities were calculated by setting the total pAd signal to 100% (shown in the *right panel*). *B*, salt sensitivity of the pAd·rTOM40 complex. The binding assay was performed as in *A* using 5 μg of rTOM40 in the presence of the indicated concentrations of NaCl. In the *lower panel*, the pAd·rTOM40 complex formed after 30 min of incubation was incubated with 500 mM NaCl (*Af*) and then subjected to the pull-down assay as in *A*. In a separate experiment, pAd and rTOM40 were incubated in the presence of 500 mM NaCl (*Bf*) followed by the pull-down assay. The quantified results are shown in the *right panel*. *C*, sequestration of the MPP-processing site of pAd within the rTOM40 molecule. pAd (1.4 μg) and rTOM40 (3.8 μg) were incubated in 50 μl at 30 °C for 30 min. The reaction mixtures were then incubated with Ni-NTA beads to separate into pAd (*unbound*) and the pAd·rTOM40 complex (*bound*). Both fractions were then incubated with (+) or without (−) MPP at 30 °C for 30 min, and the reaction mixtures were analyzed by SDS-PAGE and subsequent immunoblotting with anti-adrenodoxin antibodies. *D*, dose-dependent sequestration of the MPP-processing site of pAd by rTOM40. pAd (1 μg) and the indicated amounts of rTOM40 were incubated at 30 °C for 30 min. The reaction mixtures were then incubated with MPP at 30 °C for 30 min, which were subjected to SDS-PAGE and subsequent image analysis. The protection efficiency (%) was calculated as the ratio of pAd to pAd *plus* mAd, and shown in *E*.

by the other interactions involving hydrophobic interactions. The so-called "*cis*-binding sites" or "*cis*-sites" of mitochondria or mitochondrial outer membranes, which are located in the protease-sensitive surface receptors Tom20 and Tom22, are sensitive to salt concentrations as low as 100 mM (22–26). Therefore, the "*cis*"-site of TOM40 involved in the initial precursor recognition binds preproteins through stronger ionic interactions than that for the *cis*-binding site of the mitochondrial outer membrane. Stan *et al.* (27) demonstrated that the isolated *N. crassa* TOM holocomplex and the proteinase K-treated core not only bind pSU9-DHFR but protect the precursor from cleavage by MPP, indicating partial translocation of the precursor protein into the TOM complex and that the MPP cleavage site is protected by the TOM complex against MPP. Because this MPP protection is a suitable criterion to assess Tom40 function, we examined MPP protection with rTOM40. Recombinant pAd was incubated with rTOM40 and then the pAd·rTOM40 complex was isolated using nickel resin, which was then subjected to MPP digestion. As shown in Fig. 3*C*, the pAd recovered as the complex with rTOM40 was protected against MPP, whereas unbound pAd was efficiently processed. This protection occurred as a function of the amount of rTOM40 (Fig. 3, *D* and *E*), and the reaction was essentially saturated by 4–8 μg of rTOM40 per 1 μg of pAd (roughly calculated, ~2–4 mol of rTOM40/mol of pAd, assuming the molecular size of rTOM40 and pAd to be 38 and 20 kDa, respectively). The rTOM40-dependent MPP protection was also observed for pSU9-DHFR (data not shown). Therefore, recombinant rTOM40 had properties similar to those of the isolated *N. crassa* TOM holocomplex or the proteinase K-treated core, which is composed solely of the oligomeric form of Tom40 (27). The TOM core complex was unable to partially translocate the preprotein unless phospholipids from the mitochondrial outer membrane were supplied externally (27). Because phospholipid P_i was not detected in our rTOM40 preparation (data not shown), rTOM40 seemed to have folded correctly in Brij35 during the

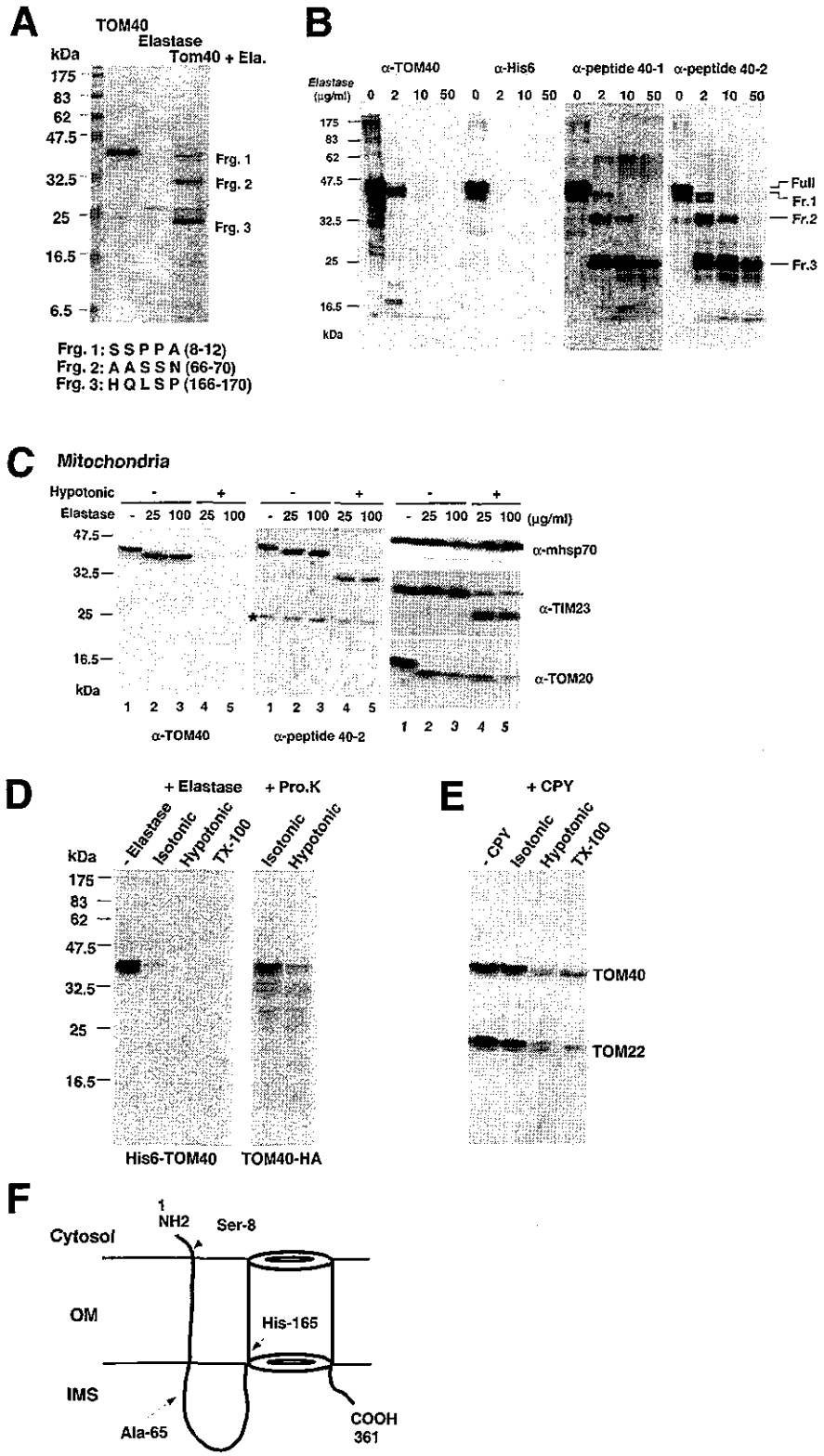

FIG. 4. **Domain structure and membrane topology of rTOM40.** *A*, elastase (*Ela*) digestion of *rTOM40*. *rTOM40* (3 μg) was digested with 2 μg/ml elastase in 50 μl at 0 °C for 30 min. The reaction mixture was trichloroacetic acid-precipitated and analyzed by SDS-PAGE and subsequent Coomassie Brilliant Blue staining. *B*, recognition of the elastase-produced fragments of rTOM40 by various antibodies. rTOM40 (3 μg) was digested in 50 μl with the indicated concentrations of elastase at 0 °C for 30 min. The reaction mixtures were trichloroacetic acid-precipitated, and the precipitates were solubilized in the loading buffer, divided into 4 aliquots, and analyzed by SDS-PAGE and subsequent immunoblotting using the indicated antibodies. *C*, elastase susceptibility of endogenous rTOM40 in the mitochondrial *outer membrane*. Mitochondria (50 μg/100 μl) were digested with the indicated concentrations of elastase at 0 °C for 30 min under isotonic (−) or hypotonic (+) conditions. The reaction mixtures were trichloroacetic acid-precipitated and subjected to SDS-PAGE and subsequent immunoblotting using the indicated antibodies. *Asterisk*, nonspecific band. *D*, membrane topology of the N- and C-terminal ends of rTOM40 in the outer membrane as probed by elastase and proteinase K (*Pro.K*). Mitochondria (10 μg/100 μl) harboring either *N-terminal* His_6-tagged rTOM40 (His_6-TOM40) or C-terminal HA-tagged rTOM40 (TOM40-HA) were treated with or without 100 μg/ml elastase or 100 μg/ml proteinase K at 0 °C for 30 min under the indicated conditions. The trichloroacetic acid-precipitates were resolved by SDS-PAGE and analyzed by immunoblotting using the antibodies against His_6 or HA. *TX-100*, Triton X-100. *E*, topology of the C-terminal end of rTOM40 in the mitochondrial outer membrane as probed by carboxypeptidase Y (*CPY*). Mitochondria (50 μg/100 μl) were treated with 5 μg/ml carboxypeptidase Y at 30 °C for 30 min under the indicated conditions. The reaction mixtures were analyzed by SDS-PAGE and subsequent immunoblotting using the indicated antibodies. *F*, schematic representation of the topology of rTOM40 in the mitochondrial outer membrane. The β-structure-enriched C-terminal half is shown as the cylindrical structure. The sites Ala^7–Ser^8 and Ala^{65}–Ala^{66} are accessible to elastase from outside mitochondria and from the intermembrane space, respectively, whereas Ile^{165}–His^{166}, which is accessible to elastase in the purified rTOM40, is resistant in the outer membrane to elastase treatment from either side of the membrane. The segment 1–165 should span the membrane at least once, although the detailed membrane disposition of this segment is not known. *OM*, outer membrane; *IMS*, intermembrane space.

purification process to acquire the activity of partial translocation of preproteins even in the absence of phospholipids.

Domain Structure of rTOM40 and Its Membrane Topology—We then probed the domain structure of purified rTOM40 using protease digestion. Elastase (2 μg/ml) treatment of rTOM40 at 0 °C for 30 min produced at least three distinct fragments (Fig. 4*A*). Fragments 1 and 2 were formed transiently, and fragment 3 was formed stably. These fragments were detected even after 50 μg/ml elastase digestion (see Fig. 4*B*). N-terminal amino acid sequencing revealed that fragments 1–3 had lost residues 1–7, 1–65, and 1–165, respectively. The antibodies against rTOM40 (α-TOM40) recognized only fragment 1, whereas two antibodies raised against the synthetic peptides corresponding to the regions near the C terminus (residues 323–345: peptide

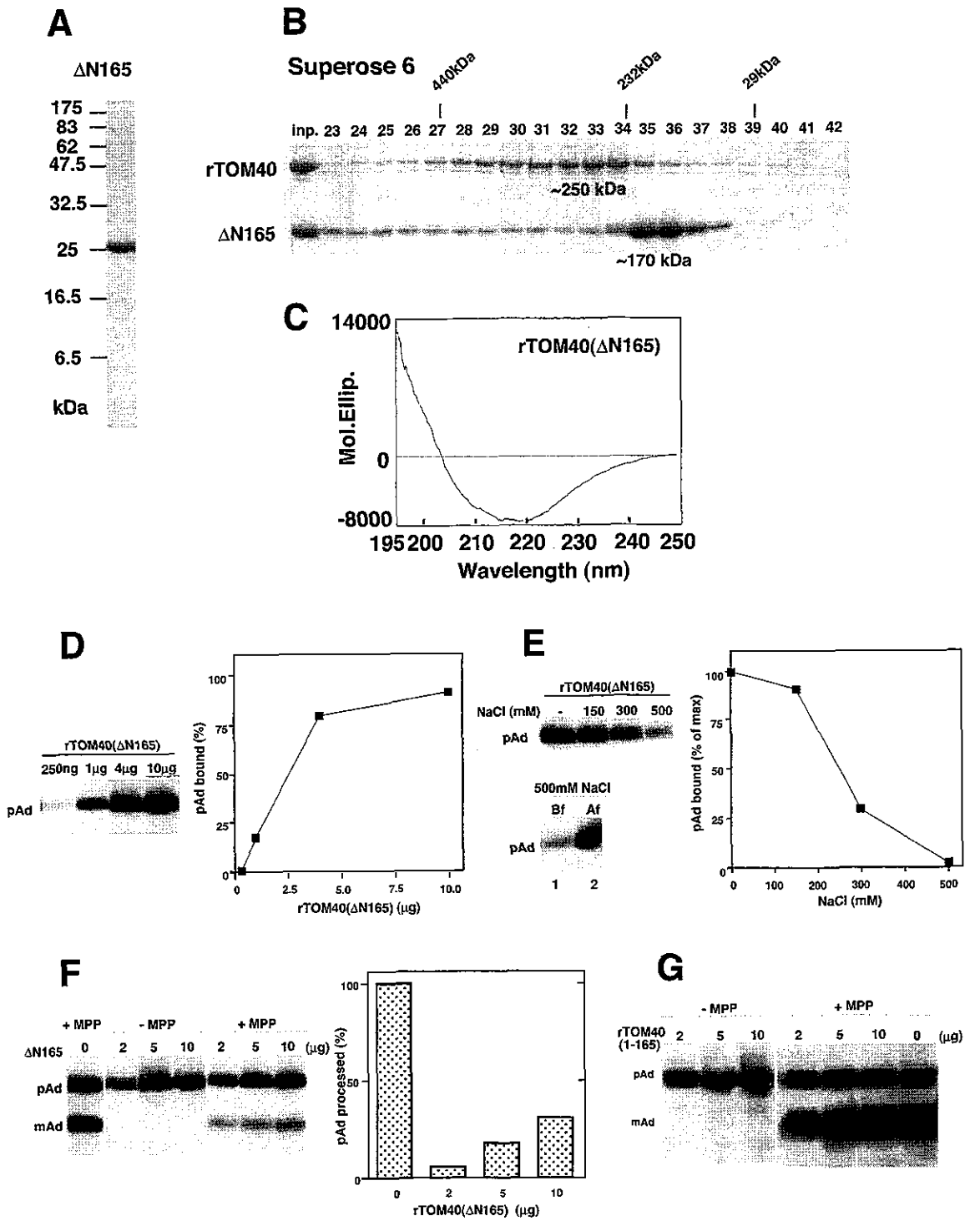

FIG. 5. **Structural characteristics of purified rTOM40(ΔN165) and its properties of preprotein recognition.** *A*, SDS-PAGE profile of purified rTOM40(ΔN165). *B*, elution profiles of rTOM40 and rTOM40(ΔN165) through Superose 6 column equilibrated with 20 mM Tris-HCl (pH 7.5) containing 0.5% Brij35 and 150 mM NaCl. *C*, CD spectrum of rTOM40(ΔN165). *D*, binding of pAd by rTOM40(ΔN165) as assessed by pull-down assay. pAd (1 μg) was incubated with the indicated amounts of rTOM40(ΔN165) (N-terminal His_6-tagged), and then the reaction mixtures were subjected to pull-down reaction. Other conditions were as described in the legend to Fig. 3. *E*, salt sensitivity of the pAd·rTOM40(ΔN165) complex. The binding assay was performed as in *D* using 5 μg of rTOM40(ΔN165) in the presence of the indicated concentrations of NaCl. *F*, sequestration of the MPP-processing site of pAd within rTOM40(ΔN165) molecule. pAd and rTOM40(ΔN165) were incubated at 30 °C for 30 min. The reaction mixtures were then incubated with Ni-NTA beads. The pAd·rTOM40(ΔN165) complex was incubated with (+) or without (−) MPP at 30 °C for 30 min, and the reaction mixtures were analyzed by SDS-PAGE and subsequent immunoblotting with anti-adrenodoxin antibodies. In a separate experiment (ΔN165 = 0 μg), pAd was incubated with MPP at 30 °C for 30 min, and the reaction mixture was analyzed by SDS-PAGE and subsequent immunoblotting. The band intensities were quantified, and the processing efficiency (mAd/(pAd + mAd)) was calculated by setting the efficiency in the absence of rTOM40(ΔN165) to 100% (shown in the *right panel*). *G*, rTOM40-(1–165) binds pAd but does not sequester the MPP-processing site within the molecule. The indicated amounts of N-terminal His_6-tagged rTOM40-(1–165) were incubated in 200 μl with 1 μg of pAd, and the reaction mixtures were subjected to the MPP protection assay as described in *F*.

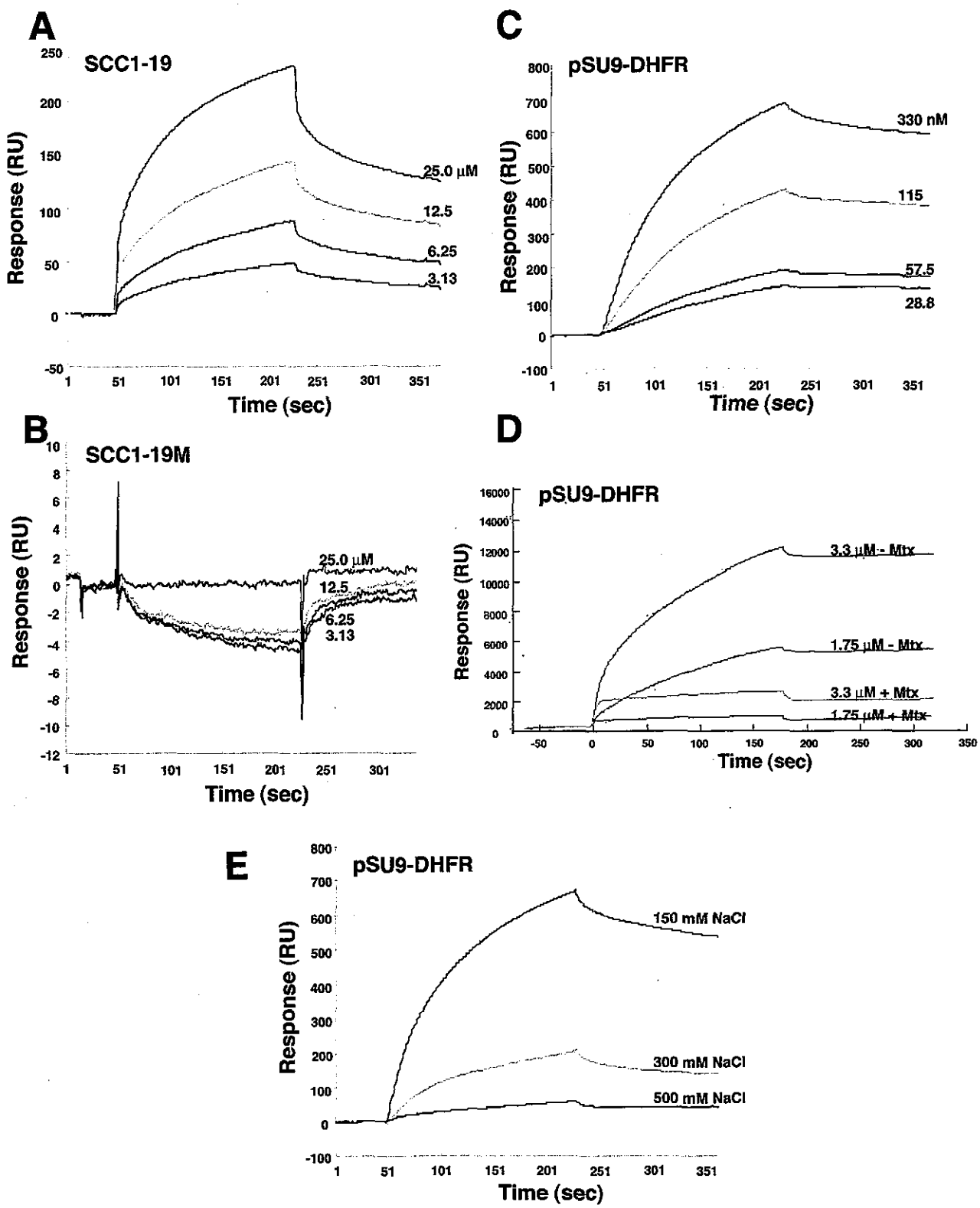

FIG. 6. **Interaction of the presequence peptide or pSU9-DHFR with rTOM40 as assessed by SPR.** *A*, SCC1–19; *B*, SCC1–19M; or *C*, pSU9-DHFR in running buffer containing 0.05% Brij35 was injected to rTOM40-immobilized sensor chip at 25 °C. *D*, pSU9-DHFR pretreated with or without methotrexate (*Mtx*) at 0 °C for 30 min was injected into the sensor chip. Other conditions were described under "Experimental Procedures." *E*, interaction of rTOM40 and pSU9-DHFR was performed in running buffer containing the indicated concentrations of NaCl.

40–1, and 189–207: peptide 40–2) recognized all three fragments (Fig. 4*B*). On the other hand, anti-His_6 antibodies only recognized the full-size rTOM40 (Fig. 4*B*). Thus, rTOM40 antibodies recognized the epitopes located within the N-terminal 65 residues of rTOM40. These results indicated that the C-terminal half of rTOM40 (residues 166–361; 21.4 kDa) folded

to form a stable domain structure.

We then addressed the topology of rTOM40 in the mitochondrial outer membrane using antibodies against rTOM40 (α-TOM40) and against a synthetic peptide corresponding to residues 189–207 (α-peptide 40-2). Elastase treatment of rat liver mitochondria under isotonic conditions produced a fragment, which was recognized both by α-TOM40 and α-peptide 40-2(Fig. 4*C*, *left* and *middle panels*). Under hypotonic conditions, elastase produced a fragment, which was detected only by α-peptide 40-2 (Fig, 4*C*, *middle panel*). From the size and reactivity with the antibodies, the bands produced under isotonic conditions and hypotonic conditions were considered to correspond to fragment 1 and fragment 2, respectively. These results indicated that the N-terminal site (Ala^7–Ser^8) of rTOM40 is exposed to the outer surface of the mitochondria, whereas the site Ala^{65}–Ala^{66} is localized in the intermembrane space. The Ile^{165}–His^{166} site, which is accessible to elastase in purified rTOM40 to produce fragment 3, was masked by the membrane or by the components of the TOM complex. The behavior of mitochondrial markers, mHsp70 (matrix protein), TIM23 (inner membrane protein extruding the N-terminal segment out of the inner membrane), and TOM20 (outer membrane protein extruding the bulk C-terminal portion to the cytosol), indicated that the protease digestion reactions were well controlled (Fig. 4*C*, *right panel*). Of note, fragments 1 and 2 were resistant to sodium carbonate (pH 11.5) extraction, indicating that they were firmly embedded in the membrane (data not shown). Topology of the N-terminal segment was further confirmed by using mitochondria isolated from HeLa cells expressing N-terminal His_6-tagged rTOM40. As shown in Fig. 4*D*, the His_6 epitope tag was removed by elastase treatment under isotonic conditions, indicating that the N-terminal segment of rTOM40 is exposed to the cytosol. We then probed the orientation of the C-terminal segment by using mitochondria harboring C-terminal hemagglutinin (HA)-tagged rTOM40. When the mitochondria were treated with proteinase K under isotonic conditions, the HA tag was unaffected, whereas it was completely removed from rTOM40 when the outer membrane was ruptured by hypotonic treatment, thus indicating that the C-terminal segment is exposed to the intermembrane space (Fig. 4*D*, *right panel*). This was further confirmed by carboxypeptidase Y treatment. rTOM40 in the isolated mitochondria was resistant to carboxypeptidase Y treatment under isotonic conditions, whereas it was completely digested under hypotonic conditions or in the presence of Triton X-100 (Fig. 4*E*). As a control, rTOM22 that is inserted into the outer membrane in the N_{out}-C_{in} orientation exhibited the same susceptibility to the carboxypeptidase Y treatment (Fig. 4*E*). Taken together, rTOM40 is embedded in the outer membrane exposing its N-terminal segment to the cytosol and the C-terminal segment to the intermembrane space, whereas at least the site Ala^{65}–Ala^{66} is exposed to the intermembrane space (Fig. 4*F*). Whether segment 1–165 is embedded in the membrane by a single or multispanning configuration remains to be determined. The predicted overall topology is distinct from that of *N. crassa* Tom40; the N- and C-terminal ends are exposed to the intermembrane space (28, 29). The N-terminal segment of *S. cerevisiae* Tom40 is exposed to the cytosol (12), but the topology of the C-terminal segment is not known.

rTOM40(ΔN165) Has a Secondary Structure and Preprotein-binding Properties Comparable with rTOM40—Based on the above findings, we purified a recombinant protein rTOM40(ΔN165) (21.4 kDa) in which the N-terminal 165-residue segment of rTOM40 was deleted, essentially according to the procedure adopted for rTOM40 (Fig. 5A). On a Superose 6 gel filtration column, it was eluted at an apparent molecular size of ~170 kDa with a sharp elution peak compared with rTOM40 (Fig. 5*B*). The secondary structure calculated from the CD spectrum in 0.5% Brij35 (Fig. 5*C*) revealed 62.0% β-sheet, 1.8% α-helix, 1.8% turn, and 34.5% random structures.

TABLE I
WT indicate wild type Kinetic parameters by surface plasmon resonance

TOM40		SCC 1–19	pSU9-DHFR
WT (full)	k_a (M^{-1} s^{-1})	3.0×10^2	3.1×10^4
	k_d (s^{-1})	8.7×10^{-4}	3.7×10^{-6}
	K_D (k_d/k_a)	3.0×10^{-6}	1.2×10^{-10}
ΔN165	k_a (M^{-1} s^{-1})	1.8×10^2	2.9×10^4
	k_d (s^{-1})	8.7×10^{-4}	2.3×10^{-5}
	K_D (k_d/k_a)	4.9×10^{-6}	8.0×10^{-10}

rTOM40(ΔN165) had preprotein-binding properties comparable with those of rTOM40 as follows: (i) dose-dependent pAd binding (Fig. 5*D*); (ii) salt-sensitive initial binding of pAd, followed by salt-resistant binding (Fig. 5*E*); and (iii) sequestration of the MPP processing site within the rTOM40(ΔN165) pore (Fig. 5*F*). It should be noted that the purified recombinant form of segment 1–165 of rTOM40 (rTOM40-(1–165)) bound pSU9-DHFR with a K_D of 1.4×10^{-10} M as assessed by SPR measurements (data not shown), but it failed to protect the precursor from attack by MPP (Fig. 5*G*), suggesting that the protection against MPP was because of specific interactions with rTOM40(ΔN165). Taken together, rTOM40(ΔN165) exhibited preprotein recognition properties as the import pore comparable with those of rTOM40. In support of these findings, rTOM40 and rTOM40(ΔN165) reconstituted into proteoliposomes exhibited permease activity for the vesicle-entrapped sucrose (see below).

Binding Kinetics of Preproteins to rTOM40 and rTOM40-(ΔN165) as Analyzed by SPR—We next measured the kinetics of interaction of rTOM40 or rTOM40(ΔN165) with either the synthetic presequence SCC1–19 or recombinant pSU9-DHFR by using SPR. rTOM40 or rTOM40(ΔN165) was immobilized to the sensor tips, and various concentrations of presequence or pSU9-DHFR were injected. The binding curves obtained (Fig. 6 for rTOM40; data not shown for rTOM40(ΔN165)) were analyzed by using BIA Evaluation software. Calculated association (k_a) and dissociation (k_d) rate constants and K_D (k_d/k_a) values are summarized in Table I. The affinity of rTOM40 for presequence peptide SCC1–19 was 3.0×10^{-6} M (Table I). No binding was observed with nonfunctional control peptides SCC1–19M (20) (Fig. 6*B*) and Synb2 (30) (data not shown). In contrast, however, rTOM40 exhibited ~10^4-fold higher affinity (1.2×10^{-10} M) for pSU9-DHFR compared with the synthetic presequence, suggesting that the mature segment of the precursor was responsible for the high affinity binding (Fig. 6*C* and Table I). When the conformation of the DHFR segment was stabilized with methotrexate, binding of pSU9-DHFR was strongly inhibited (Fig. 6*D*). Taken together, these results suggested that the affinity of rTOM40 for the presequence *per se* was rather low, and the affinity was greatly increased by the presence of the unfolded mature region of the preprotein.

We then examined the salt sensitivity of the interaction between rTOM40 and pSU9-DHFR. The interaction was salt-sensitive, and the binding was almost completely inhibited by 0.5 M NaCl (Fig. 6*E*), confirming the results of the pull-down assays (see Fig. 3). These results indicated that rTOM40 initially binds preproteins mainly through ionic interactions, which is followed by some other interactions including hydrophobic forces; the unfolded mature segment of preprotein seemed to contribute to the latter interactions (13). rTOM40(ΔN165) exhibited similar but slightly lower affinity

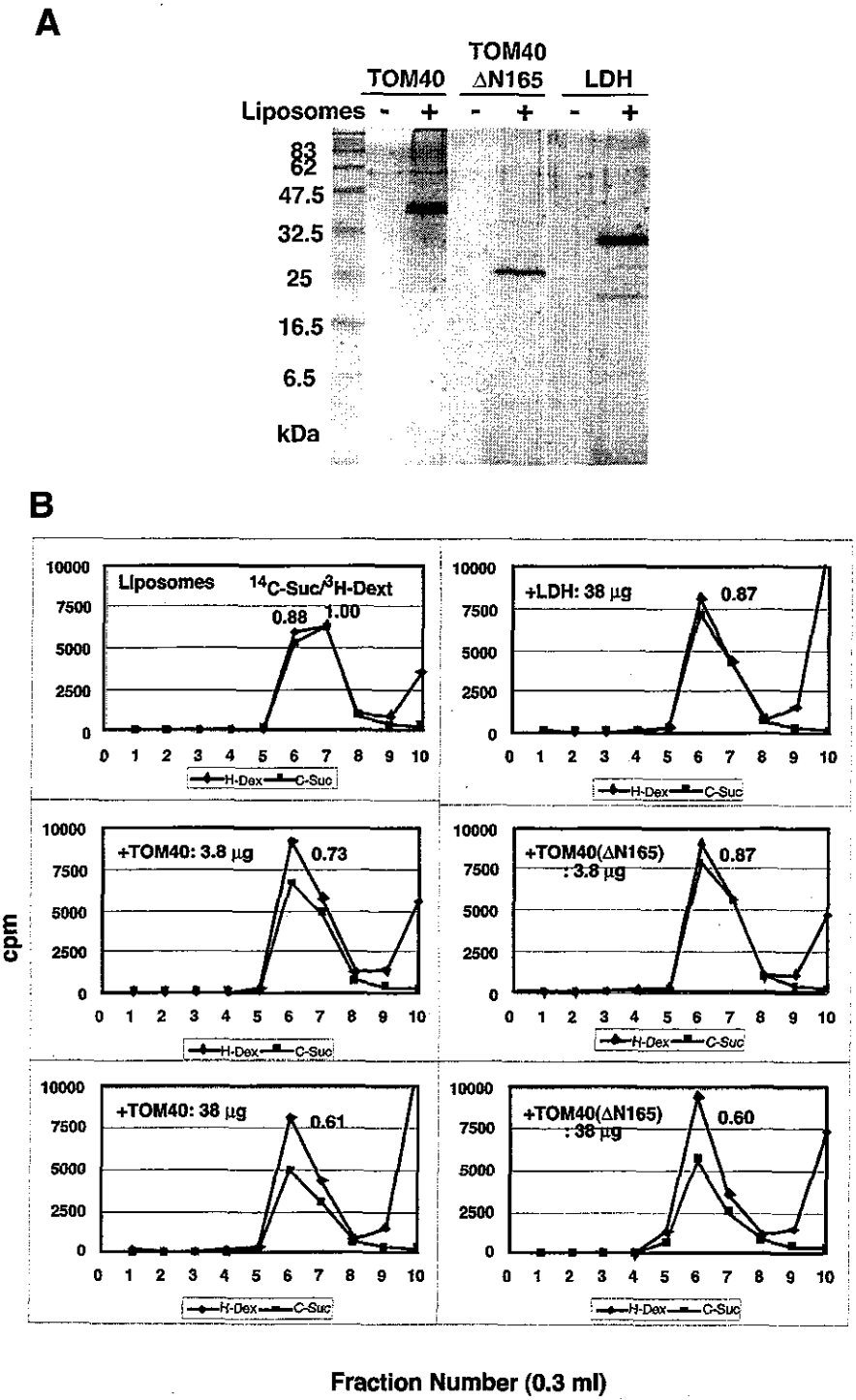

FIG. 7. **Sucrose passage activity of rTOM40 and rTOM40(ΔN165).** *A*, reconstituted proteoliposomes (*asolectin* +) or mock-treated proteins (asolectin −) were subjected to centrifugal floatation at 100,000 rpm for 90 min. The 0.25 and 1.25 M sucrose layers containing proteoliposomes were collected and analyzed by SDS-PAGE and Coomassie Brilliant Blue staining. As the control, mock-treated proteins remained in the bottom fractions of the tubes. *B*, elution profiles of the [^{14}C]sucrose- and [^{3}H]dextran-entrapped proteoliposomes. [^{14}C]Sucrose and [^{3}H]-dextran were enclosed in the proteoliposomes *reconstituted with asolectin and* the indicated proteins. The reaction mixtures were subjected to gel filtration through Sepharose CL-4B. Radioactivities of the eluted fractions were measured. The ^{14}C/^{3}H ratios of the peak fractions were normalized so that those of the incubation mixtures would be equal to 1.0. Other conditions were described under "Experimental Procedures." *LDH*, lactate dehydrogenase.

for SCC1–19 and pSU9-DHFR compared with full size rTOM40 (Table I and data not shown). The N-terminal 165 segment might contribute to stabilize the correct conformation of the pore-forming segment.

rTOM40 and rTOM40(ΔN165) Exhibit Sucrose Passage Activity When Reconstituted into Liposomes—Because our attempts to measure the channel activity for rTOM40(ΔN165) by using electrical methods were unsuccessful for technical reasons, we tried to measure the pore activity biochemically. Because the TOM complex, when reconstituted into proteoliposomes, mediates passage of small molecules (11, 31), we examined whether rTOM40(ΔN165) has sucrose passage activity, using the method adopted for measuring the activity of mitochondrial porin (17, 32). This assay measures the retention of large [^{3}H]dextran (mean M_r 70,000) *versus* small [^{14}C]sucrose that had been trapped into proteoliposomes containing rTOM40 proteins by sieving through a Sepharose 4B column. These experiments revealed that both rTOM40 and rTOM40(ΔN165) mediated passage of sucrose to a significant extent (Fig. 7 and Table II). As the controls, heat-denatured rTOM40(ΔN165) and cytoplasmic enzyme lactate dehydrogenase were inactive in this assay. We thus concluded that the

TABLE II

Release of [^{14}C]sucrose from vesicles reconstituted with TOM40 proteins

Results are normalized so that the $^{14}C/^{3}H$ ratios of the incubation mixture would be equal to 1.0. Results of three independent experiments are shown. LDH indicates lactate dehydrogenase.

Addition	Incubation mixture		Isolated vesicles		$^{14}C/^{3}H$
	[^{3}H]Dextran	[^{14}C]Sucrose	[^{3}H]Dextran	[^{14}C]Sucrose	
	cpm		*cpm*		
None	38,200	35,000	5,950	5,230	0.96
Tum40					
3.8 μg	47,900	43,300	9,070	6,640	0.81
38 μg	44,400	40,300	8,110	4,960	0.67
Tom40(ΔN165)					
3.8 μg	43,400	39,500	9,030	7,859	0.97
38 μg	47,600	41,000	9,470	5,650	0.69
Heated 38 μg	52,200	48,400	5,410	4,640	0.92
LDH					
38 μg	45,200	41,000	8,110	7,080	0.96

C-terminal half-segment of rTOM40, like full-size rTOM40, mediates passage of small molecules across the membranes. These properties seem to correspond to the ability of rTOM40 and rTOM40(ΔN165) for sequestration of the MPP-processing site of preprotein within the molecule (see Fig. 3 and Fig. 5).

DISCUSSION

Virtually all the nuclear coded mitochondrial proteins are translocated and sorted into mitochondrial subcompartments via the TOM complex; preproteins transported to the inner compartments are translocated through the TOM channel irrespective of whether they are destined to soluble compartments or to the inner membrane. On the other hand, the outer membrane proteins are sorted by the TOM complex from the proteins destined for the inner compartments and anchored to the lipid bilayer of the outer membrane. As an initial step for understanding the mechanism of this diverse preprotein recognition by the TOM channel, we purified active recombinant rTOM40, and we analyzed the recognition properties using matrix-targeted preproteins.

Purified rTOM40 bound preproteins with high affinity and sequestered the MPP-processing site within the molecule. Furthermore, when reconstituted into liposomes, it exhibited presequence-sensitive cation-selective channel activity. Therefore, recombinant rTOM40 was correctly refolded to attain the functional conformation as the preprotein translocation pore. The CD spectrum of rTOM40 did not exhibit the light-scattering effects caused by aggregated species and revealed a greater than 60% β-sheet structure. This value coincided well with that for recombinant *S. cerevisiae* Tom40 (12), although the CD spectra differed considerably. In contrast, the β-sheet structure content of *N. crassa* Tom40 predicted by CD spectra or IR spectra was markedly lower with a maximum of 31% (10). The α-helical structure of rTOM40 (10%) was half that of *N. crassa* Tom40. The reason for the difference in the secondary structure between *N. crassa* and mammals is not known.

Most importantly, this study demonstrates that the purified membrane embedded C-terminal, half-formed ~170-kDa homo-oligomeric complex with a greater than 60% β-sheet structure and exhibited preprotein-binding properties comparable with those of rTOM40, suggesting that the C-terminal segment constitutes the preprotein conducting pore. Alignment of Tom40 proteins from several organisms revealed that the sequence conservation is higher in the C-terminal pore-forming segment compared with the N-terminal segment (14). Although attempts to measure the presequence-responsive channel activity of rTOM40(ΔN165) electrically were unsuccessful, we could demonstrate that it mediated passage of sucrose across the membrane. This preparation will help analyze the structure of the pore and preprotein recognition mechanisms.

rTOM40(ΔN165) was almost functionally identical with rTOM40 with respect to the preprotein recognition, and both exhibited enriched β-sheet structures, thus the β-barrel structure is responsible for the pore function as is the case for porin (28, 33). The β-structure content of rTOM40(ΔN165) was lower (62%) than that of rTOM40. Because the random coil structure was increased in rTOM40(ΔN165), proper refolding might be disturbed to some extent. The N-terminal 1–165 segment might be required for correct formation or stabilization of the pore structure, and this might be reflected in the decreased affinity of rTOM40(ΔN165) for pSU9-DHFR.

Here we demonstrated that purified recombinant rTOM40 and rTOM40(ΔN165) exhibited virtually identical properties with the TOM core complex (24, 27). They initially bind the preprotein through predominantly electrostatic interactions and partially translocate the preprotein to the salt-resistant *trans*-site that is inaccessible to MPP, probably within the translocation channel. Stabilization of the DHFR moiety by methotrexate inhibited binding of pSU9-DHFR to rTOM40 or rTOM40(ΔN165), suggesting that the partial translocation is accompanied by unfolding of the mature segment, and the activity is restricted to the C-terminal half of rTOM40. These results also indicate that purified rTOM40 as well as rTOM40(ΔN165) contain the salt-sensitive *cis*-binding site. The salt-sensitive binding to the *cis*-site provided by the surface receptors Tom20 and Tom22 is much weaker than that in rTOM40 or rTOM40(ΔN165); *cis*-site binding of the preprotein was almost completely inhibited by 100 mM KCl (22–24). Consistent with this, the K_D values of preproteins for the cytoplasmic domain of import receptors Tom70 or Tom20 as measured by SPR were 10^{-7}–10^{-8} M (34). This affinity difference might facilitate vectorial preprotein transfer from the surface import receptors to the *cis*-binding site of Tom40.

Analysis by SPR revealed that rTOM40 bound pSU9-DHFR with high affinity (in the 10^{-10} M range), and stabilization of the DHFR moiety greatly decreased the affinity. Most interestingly, rTOM40 bound a presequence peptide but with 10^4-fold lower affinity at 3.0×10^{-6} M. These results indicate that the mature portion of the preprotein contributes significantly to the high affinity binding. It should be noted that the rTOM40·pSU9-DHFR complex or rTOM40(ΔN165)·pSU9-DHFR complex, once formed, was resistant to salt treatment, indicating a mode of interaction different from the initial interactions in the latter binding stage or in the *trans*-site binding in the purified molecules. The precise nature of the interaction of the preprotein with the *trans*-binding site remains to be determined. rTOM40 and rTOM40(ΔN165) thus possess

virtually all the preprotein-binding properties characteristic of the TOM holocomplex.

What might be the function of the N-terminal 165-residue segment? rTOM40-(1–165) was expressed in *E. coli* as a soluble form. CD spectra of the purified recombinant rTOM40-(1–165) revealed that it has 49% α-helix, 6% β-sheet, and 45% random structures. The segment consisting of residues 1–65 should span the membrane at least once, although the exact states of membrane disposition of the segment including this and up to 165 residues remains unknown. Recombinant rTOM40-(1–165) bound preprotein with an affinity on the order of 10^{-10} M mainly through hydrophobic interactions; the complex was stable in the presence of 500 mM NaCl.[2] Considering that purified rTOM40 initially binds preproteins by ionic interactions, these results suggest that the 1–165 segment functions in the later stages of preprotein translocation. In *N. crassa* Tom40, segment 41–60 (corresponds to residues 80–98 of rTOM40) is essential for proper assembly/stability of Tom40 in the TOM complex (35). In a recent report, residues 51–60 (correspond to residues 90–98 of rTOM40) and the C-terminal 3 residues (residues 321–323 which correspond to 353–355 of rTOM40) are required for assembly beyond the 250-kDa assembly intermediate of the TOM complex (36). Thus, the N-terminal 1–165 segment might also be involved in the assembly with the TOM components such as Tom22 and small Tom proteins or function as the interface of releasing outer membrane proteins from the import pore into the lipid bilayer. Another possibility is that the N-terminal 1–165 segment is required for coupling the TOM complex with the translocation of inner membrane complex during preprotein transit from the outer membrane to the inner membrane.

Acknowledgments—We thank A. Ito (Kyushu University) for providing us with purified yeast mitochondrial MPP. We also thank T. Ueda (Kyushu University) for help with CD spectrum measurements.

REFERENCES

1. Schatz, G., and Dobberstein, B. (1996) *Science* **271,** 1519–1526
2. Neupert, W. (1997) *Annu. Rev. Biochem.* **66,** 863–917
3. Künkele, K.-P., Heins, S., Dembowski, M., Nargang, F. E., Benz, R., Thieffry, M., Walz, J., Lill, R., Nussberger, S., and Neupert, W. (1998) *Cell* **93,** 1009–1019
4. Pfanner, N., and Geissler, A. (2001) *Nat. Rev. Mol. Cell. Biol.* **2,** 339–349
5. Gabriel, K., Egan, B., and Lithgow, T. (2003) *EMBO J.* **22,** 2380–2386
6. Endo, T., Yamamoto, H., and Esaki, M. (2003) *J. Cell Sci.* **116,** 3259–3267
7. Dekker, P. J. T., Ryan, M. T., Brix, J., Muller, H., Hönlinger, A., and Pfanner, N. (1998) *Mol. Cell. Biol.* **18,** 6515–6524
8. Ahting, U., Thun, C., Hegerl, R., Typke, D., Nargang, F. E., Neupert, W., and Nussberger, S. (1999) *J. Cell Biol.* **147,** 959–968
9. Model, K., Prinz, T., Ruiz, T., Radermacher, M., Krimmer, T., Kühlbrandt, W., Pfanner, N., and Meisinger, C. (2002) *J. Mol. Biol.* **316,** 657–666
10. Ahting, U., Thieffry, M., Engelhardt, H., Hegerl, R., Neupert, W., and Nussberger, S. (2001) *J. Cell Biol.* **153,** 1151–1160
11. Vasiljev, A., Ahting, U., Nargang, F. E., Go, N. E., Habib, S. J., Kozany, C., Panneels, V., Sinning, I., Prokisch, H., Neupert, W., Nussberger, S., and Rapaport, D. (2004) *Mol. Biol. Cell* **15,** 1445–1458
12. Hill, K., Model, K., Ryan, M. T., Dietmeier, K., Martin, F., Wagner, R., and Pfanner, N. (1998) *Nature* **395,** 516–521
13. Esaki, M., Kanamori, T., Nishikawa, S., Shin, I., Schultz, P. G., and Endo, T. (2003) *Nat. Struct. Biol.* **10,** 988–994
14. Suzuki, H., Okazawa, Y., Komiya, T., Saeki, K., Mekada, E., Kitada, S., Ito, A., and Mihara, K. (2000) *J. Biol. Chem.* **275,** 37930–37936
15. Jackson, M. L., and Litman, B. J. (1985) *Biochim. Biophys. Acta* **812,** 369–376
16. Nabekura, J., Omura, T., and Akaike, N. (1996) *J. Neurophysiol.* **76,** 2447–2454
17. Zalman, L. S., Nikaido, H., and Kagawa, Y. (1980) *J. Biol. Chem.* **255,** 1771–1774
18. Reed, J., and Reed, T. A. (1997) *Anal. Biochem.* **254,** 36–40
19. Meisinger, C., Ryan, M. T., Hill, K., Model, K., Lim, J. H., Sickmann, A., Müller, H., Meyer, H. E., Wagner, R., and Pfanner, N. (2001) *Mol. Cell. Biol.* **21,** 2337–2348
20. Komiya, T., Rospert, S., Koehler, C., Looser, R., Schatz, G., and Mihara, K. (1998) *EMBO J.* **17,** 3886–3898
21. Iwahashi, J., Furuya, S., Mihara, K., and Omura, T. (1992) *J. Biochem. (Tokyo)* **111,** 451–455
22. Mayer, A., Neupert, W., and Lill, R. (1995) *Cell* **80,** 127–137
23. Rapaport, D., Neupert, W., and Lill, R. (1997) *J. Biol. Chem.* **272,** 18725–18731
24. Rapaport, D., Mayer, A., Neupert, W., and Lill, R. (1998) *J. Biol. Chem.* **273,** 8806–8813
25. Kanamori, T., Nishikawa, S., Nakai, M., Shin, I., Schultz, P. G., and Endo, T. (1999) *Proc. Natl. Acad. Sci. U. S. A.* **96,** 3634–3639
26. Endo, T., and Kohda, D. (2002) *Biochim. Biophys. Acta* **1592,** 3–14
27. Stan, T., Ahting, U., Dembowski, M., Künkele, K.-P., Nussberger, S., Neupert, W., and Rapaport, D. (2000) *EMBO J.* **19,** 4895–4902
28. Court, D. A., Lill, R., and Neupert, W. (1995) *Can. J. Bot.* **73,** S193–S197
29. Rapaport, D., and Neupert, W. (1999) *J. Cell Biol.* **146,** 321–331
30. Allison, D. S., and Schatz, G. (1986) *Proc. Natl. Acad. Sci. U. S. A.* **83,** 9011–9015
31. Diekert, K., de Kroom, A. I. P., Ahting, U., Niggereyer, B., Neupert, W., Kruijff, B., and Lill, R. (2001) *EMBO J.* **20,** 5626–5635
32. Mihara, K., Blobel, G., and Sato, R. (1982) *Proc. Natl. Acad. Sci. U. S. A.* **79,** 7102–7106
33. Mannella, C., Nuewald, A., and Lawrence, C. (1996) *J. Bioenerg. Biomembr.* **28,** 163–169
34. Iwata, K., and Nakai, M. (1998) *Biochem. Biophys. Res. Commun.* **253,** 648–652
35. Rapaport, D., Taylor, R. D., Käser, M., Langer, T., Neupert, W., and Nargang, F. E. (2001) *Mol. Biol. Cell* **12,** 1189–1198
36. Taylor, R. D., McHale, B. J., and Nargang, F. E. (2003) *J. Biol. Chem.* **278,** 765–775

[2] H. Suzuki, M. Maeda, and K. Mihara, unpublished observations.

J. Anat. (2004) 205, pp135–145

Expression of amyloid precursor protein-like molecule in astroglial cells of the subventricular zone and rostral migratory stream of the adult rat forebrain

Katsunori Yasuoka, Kazuho Hirata, Akio Kuraoka, Jian-wen He and Masaru Kawabuchi

Department of Anatomy and Cell Biology, Graduate School of Medical Sciences, Kyushu University, Fukuoka, Japan

Abstract

In adult mammals, new neurons in the subventricular zone (SVZ) of the lateral ventricle (LV) migrate tangentially through the rostral migratory stream (RMS) to the olfactory bulb (OB), where they mature into local interneurons. Using a monoclonal antibody for the β-amyloid precursor protein (APP) (mAb 22C11), which is specific for the amino-terminal region of the secreted form of APP and recognizes all APP isoforms and APP-related proteins, immunoreactivity was detected in specific subpopulations of cells in the SVZ and RMS of the adult rat forebrain. In the SVZ, APP-like immunoreactivity was detected in the ependymal cells lining the LV and some of the subependymal cells. The latter were regarded as astrocytes, because they were positive for the glial markers, S-100 protein (S-100) and glial fibrillary acidic protein (GFAP). APP-like immunoreactive astrocytes exhibited strong labelling of the perinuclear cytoplasm and often possessed a long, fine process similar to that found with radial glia. The process extended to an APP-like immunoreactive meshwork in the RMS that consisted of cytoplasmic processes of astrocytes forming 'glial tubes'. Double-immunofluorescent labelling with a highly polysialylated neural cell adhesion molecule (PSA-NCAM) confirmed that the APP-like immunoreactive astrocytes in the SVZ and meshwork in the RMS made close contact with PSA-NCAM-immunopositive neuroblasts, suggesting an interaction between APP-containing cells and neuroblasts. This region of the adult brain is a useful *in vivo* model to investigate the role of APP in neurogenesis.

Key words adult neurogenesis; confocal laser scanning microscopy; glial tube; immunohistochemistry; subependymal cell.

Introduction

Mitotic active cell proliferation has been reported in specific regions of the adult mammalian central nervous system (CNS), including the subventricular zone (SVZ) of the lateral ventricle (LV) (reviewed by Alvarez-Buylla & Garcia-Verdugo, 2002), the hippocampal dentate gyrus (Palmer et al. 1997) and the olfactory neuroepithelium (reviewed by Peretto et al. 1999). Attention has increasingly focused upon the SVZ of the LV, because this region is the largest germinal zone of the adult mammalian brain, contains a steady-state population of proliferating cells and harbours neural stem cells that could be used for neuroregenerative therapy (Doetsch & Alvarez-Buylla, 1996; reviewed by Alvarez-Buylla & Garcia-Verdugo, 2002). In addition, a distinct migration pathway called the rostral migratory stream (RMS) has been identified, where neural precursors generated in the anterior horn of the SVZ migrate to the olfactory bulb (OB) and mature into local interneurons (Lois & Alvarez-Buylla, 1994; Lois et al. 1996). Of particular interest is that astrocytes in this region have an immature property that is thought to be involved in the guidance of precursor cells (reviewed by Peretto et al. 1999) or capable of proliferating itself (reviewed by Alvarez-Buylla & Garcia-Verdugo, 2002). The SVZ–RMS–OB system of the forebrain seems

Correspondence
Dr Kazuho Hirata, Department of Anatomy and Cell Biology, Graduate School of Medical Sciences, Kyushu University, Higashi-ku, Maidashi 3-1-1, Fukuoka, 812-8582, Japan. T: +81 92 642 6049; F: +81 92 642 6050; E: hirata@anat1.med.kyushu-u.ac.jp

Accepted for publication *25 June 2004*

to be a useful tool for studying the mechanisms underlying neurogenesis.

Amyloid precursor protein (APP) is an integral cell membrane glycoprotein expressed in a variety of tissues, and is abundant throughout the nervous system (Selkoe, 1994). APP produces the amyloid β protein (Aβ), which is known as the major component of senile plaques found in the brain of patients with Alzheimer's disease (Goldgaber et al. 1987; Kang et al. 1987; Tanzi et al. 1987). The non-amyloidogenic pathway of APP metabolism involves enzymatic cleavage within the Aβ sequence, and promotes release of the secreted form of APP (sAPP) (Esch et al. 1990; Sisodia et al. 1990). Interestingly, several studies of embryonic (Ohta et al. 1993; Salbaum & Ruddle, 1994) and mutant animals (Mucke et al. 1994; Zheng et al. 1995) have suggested that APP plays a crucial role in neurogenesis. More recent *in vitro studies*, using a yeast expression system, have shown that the amino-terminal region is responsible for the biological activity of sAPP (Ohsawa et al. 1997, 1999; Morimoto et al. 1998a,b), including the enhancement of neurite outgrowth (Ohsawa et al. 1997) and stimulating the proliferation of neural stem cells (Ohsawa et al. 1999). The region is also involved in synapse formation (Morimoto et al. 1998a), although the carboxyl-terminal modulates synaptic activity along with amino-terminal region of sAPP (Morimoto et al. 1998b). Thus the amino-terminal region of sAPP seems to be significantly involved in neurogenesis. A number of studies have localized APP within the nervous system and shown APP expression in a wide range of cell types, including neuronal and non-neuronal cells (Palacios et al. 1992; Banati et al. 1994; Beeson et al. 1994; Ouimet et al. 1994; Chauvet et al. 1997). The considerable variation in the distribution of APP reported by these studies is thought to be partly due to the use of antibodies targeting different regions of the APP molecule (Beeson et al. 1994). Using the monoclonal antibody (mAb) 22C11, which is specific for the amino-terminal region of sAPP, Chauvet et al. (1997) reported APP-like immunoreactivity in immature types of astroglial cells. Although the entire rostrocaudal region of the brain was examined, these authors did not report the distribution of APP in the SVZ–OB system.

In the present study using the mAb 22C11 antibody, APP expression was investigated in the adult rat forebrain, including the SVZ–OB system. APP-like immunoreactivity was detected in ependymal cells and radial glia-like subependymal cells in the SVZ, and a special type of astrocyte forming glial tubes in the RMS.

Materials and methods

Animals and tissue preparation

Adult female Wistar rats weighing 140–160 g (6–8 weeks old) were used. Animals were deeply anaesthetized with diethyl ether and pentobarbital sodium salt (50 mg kg^{-1}) and perfused intracardially with 0.01 M *phosphate-buffered saline* (PBS) at pH 7.4, followed by a mixture of 4% paraformaldehyde and 0.2% picric acid in 0.1 M phosphate buffer (PB) at pH 7.4. After removal from the skull, the brains were blocked and post-fixed for 3–4 h in 4% paraformaldehyde in 0.1 M PB and immersed overnight in 20% sucrose buffer. They were then frozen with dry-ice-isopentane. The brains were cut either sagittally or frontally into 50-μm-thick serial sections on a cryostat. Sections were collected in 0.02 M potassium phosphate-buffered saline (KPBS).

Antibodies and immunohistochemistry

The immunohistochemical procedure used here has been described previously (He et al. 2000). Briefly, non-specific binding sites were blocked by pre-incubation with 0.1% bovine serum albumin (BSA) in KPBS containing 0.5% Triton X-100 at 4 °C overnight. For immunofluorescent histochemistry of APP, sections were incubated with: (1) the primary antibody, a mouse mAb for the brain Alzheimer precursor protein A4 (APP, 22C11) (Chemicon) at a dilution of 1 : 10 in KPBS at 4 °C for 4 days; (2) the secondary antibody, a biotinylated horse anti-mouse IgG (Vector) 1 : 200 at 4 °C overnight; and (3) fluorescein iso-thiocyanate (FITC)-conjugated streptavidin (1 : 200) for binding to the biotinylated secondary antibodies at 4 °C overnight. Control sections were processed identically and in parallel; however, they were incubated with KPBS instead of the primary antibodies. No labelling of the structures was detected in these controls.

For cellular identification of the immunoreactive elements, a double-immunofluorescence procedure with S-100 protein (S-100) or glial fibrillary acidic protien (GFAP) was performed. Sections were incubated with (1) a mixture of mouse mAb to APP (1 : 10) and rabbit polyclonal antibodies (pAb) to S-100 protein (Nichirei) 1 : 5 or rabbit pAb to GFAP (Research Biochemicals International; RBI) 1 : 100, with (2) a mixture of biotinylated horse anti-mouse IgG (Vector) 1 : 200 and Texas red-conjugated donkey anti-rabbit IgG (Jackson)

Table 1 Primary antibodies used in the immunohistochemical procedures

Antibody (clone)	Source	Dilution	Species
anti-APP (22C11)	Chemicon	1 : 10	Mouse IgG
anti-S-100 protein	Nichirei	1 : 5	Rabbit IgG
anti-GFAP	RBI	1 : 100	Rabbit IgG
anti-vimentin (V9)	Chemicon	1 : 0	Mouse IgG
anti-PSA-NCAM	Dr Seki	1 : 5	Mouse IgM

1 : 200, and then with (3) FITC-conjugated streptavidin (Vector) 1 : 200 for binding to the biotinylated secondary antibodies. To demonstrate the relationship between APP-like-immunolabelled elements and neuroblasts, a double-immunofluorescence procedure for APP and highly polysialylated neural cell adhesion molecule (PSA-NCAM) was used. Sections were incubated with (1) a mixture of the mouse mAb (IgG) to APP and the mouse mAb (IgM) to PSA-NCAM (kindly provided by Dr Seki, Juntendo University, Japan) (1 : 5), with (2) a mixture of biotinylated rabbit anti-mouse IgG (Fc-specific) (Jackson) (1 : 200) and FITC-conjugated goat anti-mouse IgM (μ chain-specific) (Jackson) 1 : 200, and then with (3) Texas red-conjugated streptavidin (Chemicon) 1 : 400 for binding to biotinylated secondary antibodies. The findings of the double-immunofluorescent labelling were compared with those of the single-immunofluorescent labelling, performed using each cellular markers (Table 1) prior to the labelling of the former. No difference was observed in the morphology of the immunolabelled structures between the single and double labelling. The double-labelled sections were mounted on gelatin-coated slides with Vectashield mounting medium (Vector).

To compare APP-like immunolabelled structures with those positive for the immature glial marker, vimentin, a single-immunofluorescence procedure for APP or vimentin was used in two adjacent sections. Serial sections were incubated with (1) the primary antibody, a mouse mAb to anti-APP or mouse mAb to vimentin (V9) (Chemicon) at a dilution of 1 : 10 or 1 : 30 in KPBS, respectively, then with (2) biotinylated horse anti-mouse IgG (1 : 200) as the secondary antibody, and with (3) FITC-conjugated streptavidin (1 : 200) for binding to the biotinylated secondary antibodies.

To identify the nuclei of cells, FITC-labelled sections were counterstained with propidium iodide (PI) using Vectashield mounting medium with PI (Vector).

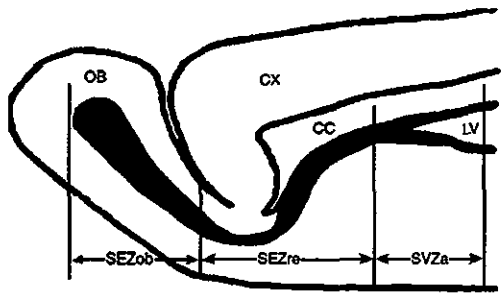

Fig. 1 Schematic diagram of a parasagittal section of the adult rat forebrain and the pathway of migrating precursor cells newly generated in the subventricular zone of the lateral ventricle. Neural precursor cells (black) are generated in the anterior horn of the subventricular zone (SVZa), migrate in a rostral direction (rostral extension of the subependymal zone; SEZre), and eventually reach the olfactory bulb (olfactory bulb portion of the subependymal zone; SEZob), thereby forming the rostral migratory stream (RMS). This schematic representation is also depicted in Figs 2, 3 and 6. LV, lateral ventricle; CX, cerebral cortex; CC, corpus callosum; OB, olfactory bulb.

Confocal laser scanning microscopy

The double-fluorescence-labelled sections were imaged using a confocal laser scanning imaging system (LSM-GB200) attached to a microscope (Olympus). Sections were illuminated by light with an excitation wavelength of 488 nm (argon laser) for FITC, and 568 nm (krypton laser) for Texas red or PI. Single and a series of optical sections were transferred separately to Channel 1 and Channel 2 to avoid crosstalk, and then superimposed. A series of optical sections at 1.5-μm intervals were projected and extended on a single plane 10–20 μm in thickness (volume projection method). Green and red images were acquired simultaneously and are either presented separately (cf. Figs 3 and 4) or as a superimposed image (cf. Figs 2 and 5).

Results

The entire length of the migration pathway for neural precursor cells from the SVZ of the LV to the OB was arbitrarily divided into three regions in a caudal to rostral direction: anterior horn of the SVZ of the LV (SVZa), rostral extension of the subependymal zone (SEZre) and olfactory bulb portion of the subependymal zone (SEZob) (Fig. 1).

In parasagittal sections, the distribution of APP-like-immunoreactive (-ir) structures was clearly observed in conjunction with PI-nuclear staining; the APP-like-ir

components consisted of cells with a prominent cellular configuration in the SVZ (Fig. 2A) and an elaborate network in the RMS (Fig. 2C,D). In the SVZa of the LV, there was intense APP-like immunoreactivity in the perinuclear region of a number of ependymal and subependymal cells (Fig. 2A,B). The subependymal cells often exhibited a similar profile to that of radial glia: rostrally, they extended a long thin process across the wall of the LV into the periventricular parenchyma. These processes were connected with the APP-like-ir network distributed throughout the RMS, including the SEZre (Fig. 2C) and the SEZob (Fig. 2D). The APP-like-ir network was predominant in the SEZre and the most rostral region of the SEZob, due to the dense distribution and more intense immunostaining of the cells. In the most rostral region of the SEZob, the processes of the APP-like-ir network spread out in a fan-shaped manner (Fig. 2D). In some areas of the RMS, a cluster of residual ependymal cells, i.e. a remnant of the olfactory ventricular wall, was occasionally observed as reported by Peretto et al. (1997). These ependymal cells exhibited strong immunoreactivity and were connected with the APP-like-ir network (Fig. 2C).

To identify APP-like-ir cells, double-immunofluorescent labelling for APP and one of the glial markers, S-100 or GFAP, was performed in coronal sections. In the SVZa, APP-like-ir ependymal and subependymal cells were positive for S-100 (Fig. 3A–C) or GFAP (Fig. 3D–F). Furthermore, a comparison of the morphology and distribution of two adjacent coronal (Fig. 3G,H) and parasagittal (Fig. 4A,B) sections revealed that APP-like expression in the SVZa matched that of vimentin, a marker of immature glial cells. Thus, APP-like-ir subependymal cells are probably an immature type of astrocyte. In the core of the SEZre, the APP-like-ir elements were also positive for S-100 (Fig. 5A–C) or GFAP (Fig. 5D–F). APP-like immunoreactivity was mainly detected within the processes, rather than the perinuclear regions, of S-100-ir astrocytes, which form 'glial tubes' in the core of the RMS (Fig. 5A–C). APP-like-ir processes completely overlapped the GFAP-ir processes. APP-like immunoreactivity was slightly stronger in the central region compared with the periphery, whereas GFAP immunoreactivity was somewhat stronger in the periphery (Fig. 5D–F). Thus, APP-like immunoreactivity was only detected in ependymal cells and subependymal astrocytes of the SVZ, and in the astrocytes forming glial tubes in the RMS.

Double-immunofluorescent labelling of coronal sections for APP and PSA-NCAM, a marker of migrating neuroblasts (Bonfanti & Theodosis, 1994), was performed to determine the relationship between APP-like-ir cells and neuroblasts migrating from the SVZ to the OB. In the SVZa, PSA-NCAM-ir elements usually formed a cluster under the layer of APP-like-ir subependymal cells, and were roughly enclosed by loose APP-like-ir networks. PSA-NCAM-ir elements sometimes made contact with APP-like-ir elements (Fig. 6A). In the SEZre, PSA-NCAM-ir elements were more numerous and closely packed in the APP-like-ir networks of glial tubes. In the core of the SEZob, PSA-NCAM-ir elements were also densely packed in APP-like-ir networks (Fig. 6B,C). Thus, PSA-NCAM-ir elements and APP-like-ir networks in the RMS always showed close apposition. In the SEZob, clusters of PSA-NCAM-ir elements were distributed beyond the limits of the core and spread towards the internal granular layer, which exhibited radial migration of neuroblasts (Fig. 6B,D). The cellular localization of PSA-NCAM was confirmed by immunofluorescent labelling of PSA-NCAM and nuclear staining with PI. PSA-NCAM immunoreactivity was observed in cells possessing round and densely stained nuclei, a characteristic of neuroblasts (Fig. 6E).

Discussion

In this study we used the antibody mAb 22C11, which is specific for the amino-terminal region of sAPP (the epitope is localized between residues 66 and 81 of APP) and recognizes all APP isoforms (Hilbich et al. 1993). Slunt et al. (1994) identified cDNA that encodes a 751-amino acid APP-like protein (designated APLP2) in the

Fig. 2 Pseudocolour three-dimensional images reconstructed from a series of 20 sections of immunofluorescent labelling for APP (green) and nuclear staining for PI (red) in the SVZa (A, B), SEZre (C) and SEZob (D) in parasagittal sections of the rat forebrain. (A) In the SVZa, a large number of ependymal and subependymal cells express strong APP-like immunoreactivity in the perinuclear region. Some of the subependymal cells rostrally extend a single, long APP-like-ir process from the cell body. (B) Higher magnification of the white box in A shows APP-like-ir processes of subependymal cells extending across the wall of the LV into the periventricular parenchyma (arrows). (C) In the SEZre, a well-developed APP-like-ir network can be seen in the region of a dense population of PI-stained nuclei in the RMS. Arrow shows that the APP-like-ir network connects with a cluster of APP-like-ir residual ependymal cells. (D) In the SEZob, the APP-like-ir processes spread out in a fan-shaped manner in the most rostral part of the RMS. Scale bars = 10 μm.

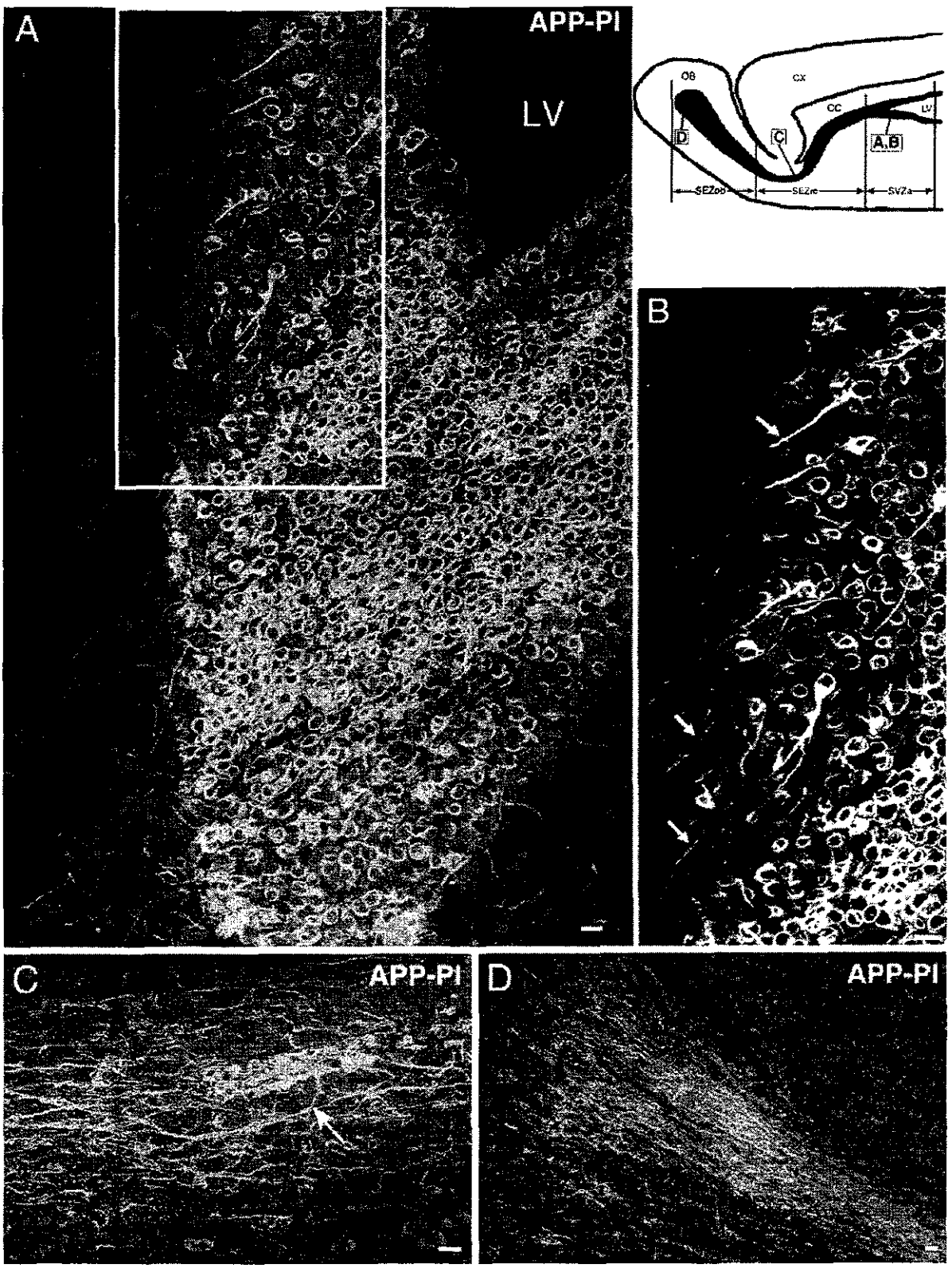

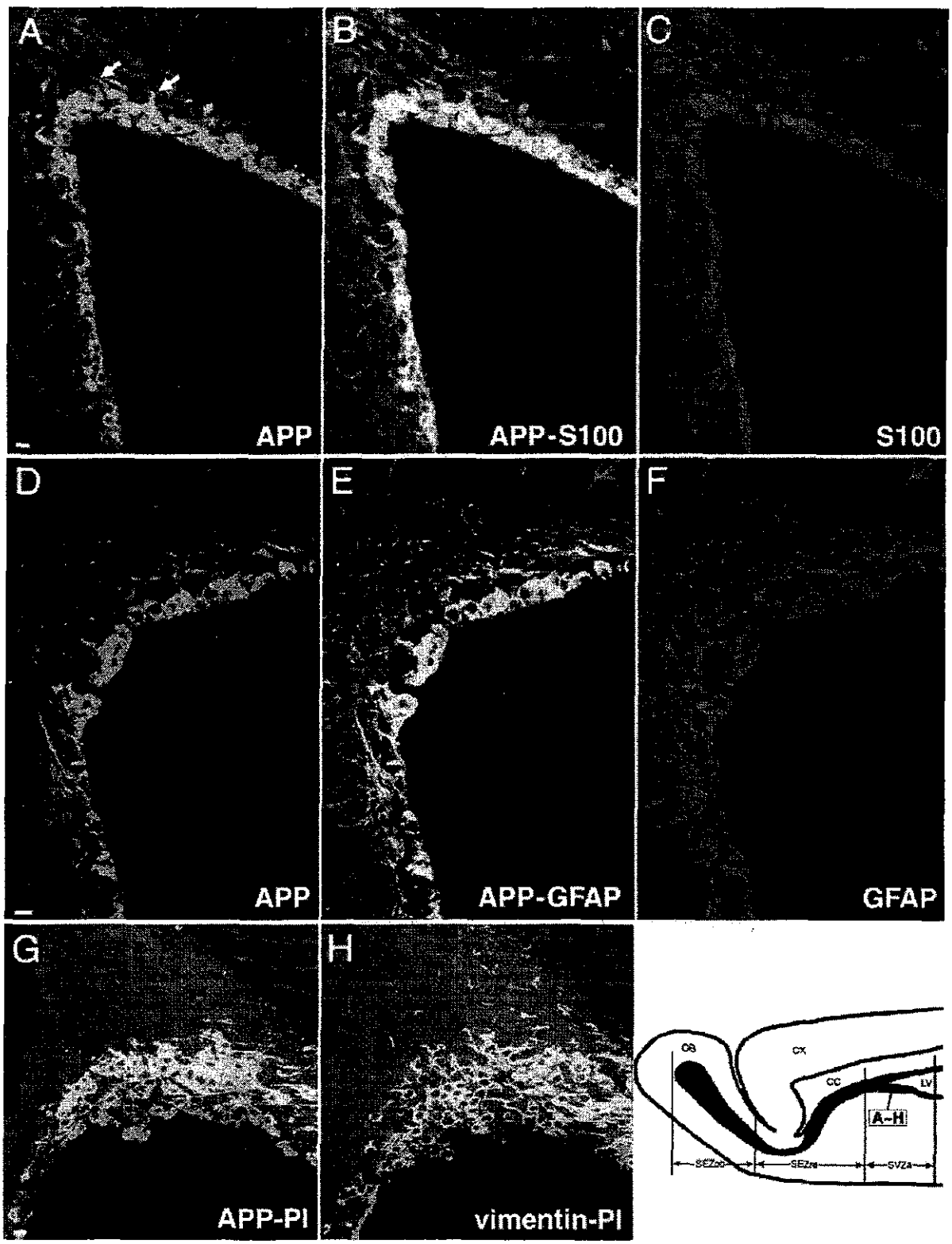

mouse and showed that the mAb 22C11 cross-reacted with mouse APLP2. It cannot be ruled out that the immunoreactivity shown here is not only for APP, but also for APLP, because rat APLP2 has approximately 95% sequence homology with the murine CDEI binding protein (Sandbrink *et al.*, 1994). Hence the immunoreactive site was designated APP-like. In the rat SVZ–OB system, mAb 22C11 immunostaining was detected in specific subpopulations of cells of both the SVZ and the RMS.

In the SVZ, at least two types of APP-like-ir cells were detected: ependymal cells that face the ventricular cavity, and subependymal cells that are located beneath the ependymal cells. The former were immunopositive for S-100 or GFAP, which may include a few tanycytes, i.e. ependymoglial cells, because Doetsch et al. (1997) reported that GFAP-positive tanycytes were occasionally observed in the SVZ. The mAb 22C11 immunostaining in ependymal cells was not confined to this specific region, but detected throughout the lining of the LV (data not shown). The APP-like immunoreactivity of the ependymal cell is consistent with that reported by Chauvet et al. (1997), although they did not describe immunoreactivity in the SVZ. The APP-like-ir subependymal cells were also positive for S100 or GFAP. According to the cellular identification of Doetsch et al. (1997), these cells were regarded as a type of astrocyte. Comparison of two adjacent sections showed that these cells approximately correspond to cells positive for vimentin, which is the major cytoskeletal component in immature glia (Dahl et al. 1981). Furthermore, confocal laser scanning microscopy revealed that APP-like-ir astrocytes often had a long process extending rostrally, and resembled that of radial glia. Although we are not able to state definitely whether these cells are radial glia, APP-like expression in the radial glia-like cells in SVZ of adult rat forebrains is not incompatible with the expression of this molecule in radial glia of the fetal and early postnatal mouse brain (Trapp & Hauer, 1994) and in rat neonatal radial glia-like structures

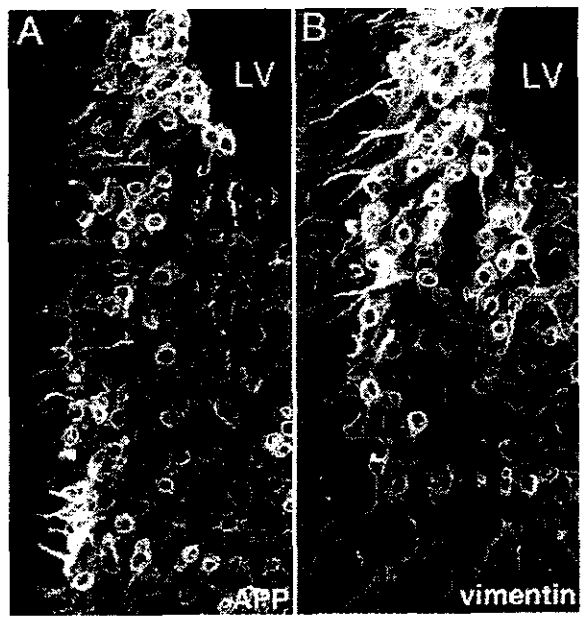

Fig. 4 Greyscale three-dimensional images reconstructed from a series of 20 sections of immunofluorescent labelling for APP (A) and vimentin (B), in two adjacent parasagittal sections of the SVZa. Rostrally directed, long processes of vimentin-ir cells are clearly shown in this parasagittal section (B), whereas the processes of the APP-like-ir cells are apparently shorter, because of being cut in the adjacent section (A).

(Chauvet et al. 1997), the former of which was examined by an mAb raised against the carboxy-terminal region. With regard to the morphology of the astrocytes in the SVZ, there seems to be the difference between the rat and mouse. Astrocytes in the mouse are positive for vimentin (Doetsch & Alvarez-Buylla, 1996), although they exhibited no immunostaining for RC 2 mAb, another marker of radial glia (Gates et al. 1995). However, there is no evidence of a long process, characteristic of radial glia, even in a three-dimensional reconstruction of ultrathin sections (Doetsch & Alvarez-Buylla, 1996; Doetsch et al. 1997). In the mouse SVZ, neuroblasts are thought to traverse a complex network of interconnected pathways formed by astrocytes to enter the

Fig. 3 (A–F) Pseudocolour images of double-immunofluorescent labelling for APP with the glial markers S-100 (A, B, C) and GFAP (D, E, F), in coronal sections of the SVZa. (A–C) Images of FITC-labelled APP-like-ir elements (A) and Texas red-labelled S-100-ir elements (C), and their superimposed image (B), of a single optical section. (D–F) Images of FITC-labelled APP-like-ir elements (D) and Texas red-labelled GFAP-ir elements (F), and their superimposed image (E), of a single optical section. In the SVZa, almost all of the APP-like-ir cells express both S-100 (yellow and yellowish green in B) and GFAP (yellow and yellowish green in E). Note that APP-like expression is confined to the S-100-ir or GFAP-ir elements within the SVZ. Arrows indicate the process extending from the APP-like-ir subependymal cells. (G, H) Pseudocolour three-dimensional images reconstructed from a series of ten optical sections of immunofluorescent labelling for APP (G), and vimentin (H), a marker of immature glial cells, in two adjacent coronal sections of the SVZa. The distribution of the APP-like-ir elements (green and yellow in G) and vimentin-ir elements (green and yellow in H) is very similar. Red indicates PI-stained nuclei. Scale bars = 10 μm.